Solid Rocket Motor Internal Flow Solutions with FlightStream®

by

Griffin DiMaggio

A thesis submitted to the Graduate Faculty of
Auburn University
in partial fulfillment of the
requirements for the Degree of
Master of Science

Auburn, Alabama
August 7, 2021

Approved by

Dr. Roy Hartfield Jr., Chair, Woltosz Professor Department of Aerospace Engineering
Dr. Anwar Ahmed, Professor Department of Aerospace Engineering
Dr. David Scarborough, Assistant Professor Department of Aerospace Engineering

Abstract

This thesis seeks to advance the state of the art for conceptual and preliminary design of solid propellant rocket motors by adapting surface vorticity solution methods to the internal ballistics problem. The practical approach is to adapt a surface-vorticity solver known as FlightStream® originally designed for external flow analysis to the solution of internal flows of interest to the solid rocket motor design community. This work focuses particularly on solid propellant rocket motor combustion chambers. Four analytic models were derived and used to validate various simple solid rocket motor internal flow models. Excellent agreement between the analytic solutions and FlightStream® was observed. The Space Shuttle's Reusable Solid Rocket Motor (RSRM) was used as a more complex and realistic validation case. To compare with the validation data, corrections to FlightStream®'s potential solution were necessary. Analyses were conducted to ensure FlightStream® produced a valid potential solution for the RSRM. The corrected solution was accurate to the validation data, though error increases in the second half of the RSRM. This was believed to be due to the radial slots between the RSRM segments, which likely generate recirculation that could not be accurately captured in the method applied in this report.

Acknowledgments

I would like to express my gratitude to my advisor, Dr. Roy Hartfield Jr., who has provided invaluable wisdom throughout my graduate studies and research, given me an excellent opportunity for my professional development, and who's patience and encouragement has been pivotal in my growth.

I would also like to thank the CEO of Research in Flight, Dr. Vivek Ahuja, who has gone above and beyond assisting me in my research, providing active feedback, and swiftly improving FlightStream® by removing bugs and adding entirely new features for the benefit of my research.

Of course, I am always thankful for my family who has always been supportive in my studies and my life. My mother, Leslie DiMaggio, and father, Jon-David DiMaggio, who have always put my needs before their own. My grandfather, Dr. James Patterson, for encouraging me to pursue my dreams of graduate studies and serving as a role model for my path as an engineer. To the many more in my family, if you are reading this, know I am beyond thankful for the love we share every day.

Table of Contents

List of Tables

List of Figures

Nomenclature

SPRM = solid propellant rocket motor

SRM = solid rocket motor

AP = ammonium perchlorate

SPP = Solid Performance Program

CFD = computational fluid dynamics

DNS = direct numerical simulation

RANS = Reynolds-Averaged Navier-Stokes

URANS = unsteady Reynolds-Averaged Navier-Stokes

LES = large eddy simulation

RSRM = Reusable Solid Rocket Motor

ρ = density

u = velocity

$\forall$ = volume

A = area

δ = solid-fuel regression rate

Φ = velocity potential

β = velocity ratio, u_h/u_b

F,G = intermediate functions

υ = separation constant

Ψ = stream function

α = taper angle

s = tapered surface

w = planar model width

P = pressure

P_0 = stagnation pressure

q = dynamic pressure

γ = specific heat ratio

R = gas constant

T_f = flame temperature

a_0 = speed of sound

a = temperature coefficient

n = pressure exponent

ζ_{comp} = compressibility correction

R_{avg} = average radius of RSRM middle segments

Ω = vorticity

Sub/Superscripts

b = burning surface

h = chamber head

1 Introduction

The following section aims to give a basic understanding of solid propellant rocket motor fundamentals, the culmination of which is to highlight the importance of internal ballistics in motor design. Insight is given on physical complexities that make experimental data gathering and internal ballistics modeling challenging. Various methods of internal ballistics modeling are introduced from low-order models to highly accurate models. Lastly, the motivation for this thesis is delineated.

1.1 Solid Propellant Rocket Motor Overview

Solid propellant rocket motors (SPRM), also referred to in the literature as solid rocket motors (SRM), are characterized by the use of solid propellant. The propellant is stored in the combustion chamber typically with a perforation down the central axis. Self-sustained combustion of the propellant begins with the activation of an ignitor, usually located at the headend of the combustion chamber. Upon ignition, a flame will form and propagate across the exposed propellant surface. As the flame covers the entire surface, the chamber pressure increases until a quasi-steady flow state is achieved. This is known as flame spreading and chamber filling, respectfully, and occurs on the order of milliseconds.[1] The combustion gases flow through the port toward the nozzle gaining momentum as mass is injected into the flow. The gas is then accelerated and expelled out of the nozzle to produce thrust.

Solid propellant rocket motors burn to completion once ignited, are generally not throttleable, and are almost always nonreusable (NASA's Space Shuttle booster being an exception). The most common applications for SRMs are boosters for space launch vehicles, high-altitude motors, and missile motors. They are also used as gas generators (focused on

creating high pressure rather than thrust) in applications like pilot emergency ejections or automotive airbags.

Theoretically, the grain regresses normal to the burning surface as it burns, though effects like erosive burning can cause nonparallel regression. The internal flow near the burning surface is highly turbulent as a result of the combustion process and viscous forces. First postulated by Taylor,[2] the injection mechanism of the propellant promotes rotationality in the flow. Even if the flow were to be inviscid, any slip boundary that should form along the burning surface would be promptly shed as new mass is injected. This no-slip boundary is caused primarily by mass injection rather than viscous forces (though these forces are still present). High velocity gases passing beside the nearly stagnant flow at the burning surface generate vorticity. Viscosity tends to dampen the strength of these vortices. Nevertheless, the rotational energy in the flow leads to higher kinetic energies concentrated near the chamber's central axis and a total pressure loss along the burning surface.

A variety of solid propellant chemical formulations are used in rocket motors. Chemical ingredients with high densities, low gas phase molecular weights, and high flame temperatures are preferred for performance. Double-base propellants are homogeneous propellant grains, the most common being the colloid formed from nitrocellulose and nitroglycerin. The performance of these propellants can be improved by adding nitramines or an elastomeric binder. Double-base propellant is typically only used in small missiles. Composite propellants are by far the most commonly used class of solid propellant. These heterogeneous propellant grains consist of a crystalized oxidizer and powdered fuel, usually ammonium perchlorate (AP) and aluminum (Al), respectfully, bound by a synthetic rubber. The performance of composite propellants can be enhanced by adding high energy plasticizer or nitramine. These modifications have the

additional benefit of reducing smoke (caused by metal oxides) from the exhaust. AP and Al can be added to double-base propellants to produce what is known as composite-modified double-base propellant. Each propellant offers its own advantages and disadvantages; an optimum propellant for a given application will depend on the specific design criteria.[3]

Along with propellant type, motor performance is governed by the grain's geometrical configuration. The chamber pressure, and therefore the motor's performance, is dependent on the burning surface area of the propellant. As the grain regresses, the exposed surface area changes, resulting in changes to the pressure. There are three classifications of grain configurations based on thrust-time (or pressure-time) characteristics: neutral burning, progressive burning, and regressive burning. The thrust remains approximately constant with time for a neutral burning configuration, increases with time for a progressive burning configuration, and decreases with time for a regressive burning configuration. Most grain configurations have a cavity through the central axis, apart from end-burning grains; common configurations include a basic tube, slotted tube, star, and wagon wheel. Some configurations utilize multiple cavities known as multiperforated grains. Three-dimensional grains burn both radially and longitudinally; examples include the finocyl configuration (fins around the central perforation) and the conocyl configuration (cone around the central perforation). Most modern designs use combinations or variants of known configurations to reduce the chance of stress cracking or instabilities occurring.

Combustion in a SRM is extremely complex and not well understood. A thin layer (~1 μm) just beneath the burning surface of the propellant, known as the degradation zone, vaporizes and degrades into smaller molecules. A small layer beneath the degradation zone is heated through conduction and the rest of the propellant remains approximately at its initial temperature. In

double-base propellants, the flame structure is homogeneous and quasi-one-dimensional. Most of the reaction occurs in a bright flame displaced from the burning surface. Between the bright flame and the burning surface is a "dark" reaction zone that emits infrared light. The flame of a composite propellant appears attached to the burning surface, with no infrared zone in-between. Due to the heterogeneous nature of the burning surface, the flame structure is unsteady and three-dimensional. Experiments have observed liquid and gaseous intermediate products, three-dimensional microstructures in the flame, aluminum agglomerates, temporally and spatially dependent processes, as well as other complexities that make accurately modeling the combustion process exceptionally difficult. Despite this, the combustion process itself is not usually a primary concern in design because extremely high combustion efficiencies are achieved in a rocket motor. More attention is often directed toward managing combustion and preventing combustion instabilities.[3]

Unstable combustion results in pressure oscillations, or acoustic instabilities, that increase the propellant burning rate, consequently increasing thrust. This can interfere with the motor's trajectory or cause potentially catastrophic internal damage. The acoustic cavity in a SRM is continuously increasing in volume with time; this has a damping effect on acoustic instabilities and oscillations generally subside as the cavity expands. Even so, motor stability is of critical importance and must be addressed in the design process. Acoustic instability analyses become more difficult as the geometrical complexity of the grain increases. Near the end of a motor's operation, low frequency waves often occur, causing unsteady bursts of combustion followed by nearly stagnant flow, otherwise known as chuffing.[3] Another form of instability in SRMs is vortex-shedding, which typically occurs due to grain slots or overhangs. The propellant grain in large motors is often segmented for ease in manufacturing. Between two grain segments is

typically a radial slot in which flow is injected into the main flow at a faster rate than from the burning surfaces just forward and aft of the slot. This injecting flow essentially restricts the upstream flow, causing a rise in pressure upstream and a suction pressure downstream. Turbulence forms as the main flow interacts with the flow injected from the slot, resulting in vortices that are shed downstream. A recirculation zone typically forms on the aft side of these grain slots.[4] Vortex shedding can also occur over grain steps, or sudden decreases in the port's cross-sectional area. The shed vortices can interact with acoustic instabilities, resulting in even greater nonlinearity in the flow.[5]

A substantial pressure differential across a grain slot or overhang can lead to structural warping known as grain deformation. This has also been observed to occur in submerged-nozzle designs, where the nozzle is positioned slightly inside of the propellant bore. The cavity formed between the nozzle and the propellant grain can experience a pressure differential that causes the grain to tighten around the nozzle. This results in higher flow velocities, a larger pressure differential, and consequently more grain deformation.[6] In some cases, this can lead to motor failure.

Another complication, particularly with submerged nozzles, is the accumulation of slag, or aluminum oxides that become trapped in the cavity created between the nozzle and grain. Aluminum in propellant tends to cling to the burning propellant surface before igniting. These particles sometimes accumulate by either melting or sintering together in the heat of the combustion reaction. Once specific conditions are met, the agglomerate ignites and enters the flow.[7] As the agglomerates reach the nozzle, some enter the cavity and become trapped by the recirculating flow. Spontaneous ejection of the aluminum agglomerates from the cavity can occur, inducing thrust perturbations that diminish motor performance.[8]

Hot combustion gases flowing with sufficient velocity across the burning surface can augment the burning rate, which is known as erosive burning. This is typically most pronounced in the early stages of operation when the port-to-throat area ratio is the smallest. Erosive burning is often more prominent in nozzleless motors.[9] In these motors, the "nozzle" is created by the propellant geometry itself. Flow expansion is generally achieved with a taper on the aft end of the propellant. In proper operation, sonic conditions are met just before the taper, which is representative of the nozzle throat. Because the flow velocity is so much higher in the chamber of a nozzleless motor, more erosive burning occurs. The most sensitive area to the erosive burning is the throat. The unparallel burning caused by the erosion can degrade the throat, sometimes shifting its geometrical location or even creating two throats. Erosive burning can cause over-pressurization in the early stages of motor operation or premature exposure of structural surfaces to hot gases in later stages, both of which can result in structural failure.[10]

1.2 Internal Ballistics Modeling

The study of propulsion, encompassing all the afore-mentioned processes, is known as internal ballistics. Understanding the internal flowfield provides valuable information that facilitates design decisions, such as geometrical configuration and propellant formulation. Ballistics analyses are necessary to ensure efficient engineering throughout the design process. The extreme conditions in a SRM created by the combustion process impose a limit on data that can be collected experimentally. Experiments can also be costly, as SRMs are generally made to be single-use. Cold flow testing is a common experimental procedure that allows for internal flow data to be obtained that would otherwise be unobtainable in the harsh environment of a combustion gas flow.[11] Likewise, the simplicity of cold flow may be preferable in

computational or analytical models intended for preliminary design for the purposes of verification and validation of solution methods.

One of the most well-known analytic cold-flow models is the Taylor-Culick solution,[12] which represents the steady, incompressible, quasi-viscous, and rotational flow in a porous cylindrical chamber. The Taylor-Culick profile has been verified as an accurate representation of the bulk-flow in a SRM through many computational, experimental, and theoretical studies.[13] In more recent works, it has been augmented to account for compressibility effects,[14] grain taper,[15],[16] wall regression,[17] and arbitrary headwall injection.[13] Predating the Taylor-Culick profile is the irrotational equivalent known as the Hart-McClure profile.[18],[19] Kelvin's minimum energy theorem predicted that this irrotational solution would have the least energy of any incompressible flow with corresponding boundary conditions. This was later confirmed by Saad & Majdalani[20] with the use of the Lagrangian optimization principle, who also uncovered a spectrum of energy states linking the potential and rotational solutions, of which the Taylor-Culick solution was found to be an equilibrium state entailing the most entropy. A clear advantage of analytical models is the immediacy of acquiring a solution (given the model has been formulated). Contrarily, analytical models are severely limited by the boundary conditions, or grain geometry, and often only describe basic configurations. The linearity of the irrotational solution may be useful in this regard, as its simplicity could allow for the application of more complex boundary conditions.[21]

Computational models allow more geometrical freedom at the expense of time. Of course, as the physical intricacy (and accuracy) of a model increases, so does the computation time. In early design, lower order solutions are typically favorable to the lengthy computation times of high-fidelity models, and often, lower order models can provide the critical performance parameters

of interest in motor design. The Solid Performance Program (SPP) is a computational tool for motor development widely used for performance prediction as well as post-test analysis.[22] SPP can take as input a three-dimensional, two-dimensional, or axisymmetric grain design, allowing faster computation times for simpler geometries. The internal ballistics module uses an element method to divide the domain into a series of elements and solve one-dimensional gas dynamic relationships in each element, while considering stagnation pressure loss and erosive burning effects. Calculation of the total pressure loss includes a correction for two-dimensional and compressibility effects.[23] Generally, the flow in a SRM is nearly one-dimensional, and one-dimensional models have shown to give acceptable fidelity for initial conceptual design assessments in many cases. However, one-dimensional methods have been observed to substantially over-predict pressure drop in motors involving complex geometries, such as those with tapered aft sections.

Solutions of greater fidelity can be obtained with two-dimensional or three-dimensional computational fluid dynamics (CFD). Many numerical techniques are employed to computationally solve the Navier-Stokes equations, which mathematically express the conservation of mass, momentum, and energy to describe the motion of fluid; common techniques include the finite difference, finite volume, and finite element methods. Direct numerical simulation (DNS) numerically solves the time-dependent Navier-Stokes equations over the entire range of spatial and temporal scales of turbulence.[24] This is the most resolved form of flow simulation and is so computationally intensive that it is generally not viable for engineering applications. DNS is restricted to low Reynolds number and simple geometry applications.

The most commonly used models in CFD are Reynolds-Averaged Navier-Stokes (RANS) equations,[25],[26] which are the time-averaged equations of motion. The RANS momentum equation contains Reynolds stress terms that are computed using a turbulence model. The complexity and fidelity of the turbulence model is based on the number of transport equations solved along with the RANS equations. Many turbulence models have been developed with a wide range of accuracies; the most common of these is the k-ε turbulence model that contains two transport equations for turbulent kinetic energy and the rate of dissipation of turbulent kinetic energy. The unsteady Reynolds-Averaged Navier-Stokes equations (URANS) are more costly than the steady-state RANS, but are useful in modeling periodic motion or other transient behavior.[27]

Greater accuracy can be obtained than with RANS or URANS with the use of large eddy simulation (LES).[28],[29] In this type of simulation, the smaller spatial scales of turbulence are filtered while the larger scales are solved directly. The flow cannot be considered steady in LES and the mesh requires high resolution, fundamentally raising computational cost. The turbulence models used to resolve the sub-grid scale stresses are often simpler and more universal than those used in RANS. A common practice is to hybridize the RANS and LES models. Doing so retains the efficiency of RANS while also gaining the benefit of the increased accuracy of LES. Typically, in this hybridize form, LES modeling would be used away from the walls while RANS is used near walls; this is known as detached eddy simulation (DES). Rocstar Multiphysics is a popular fully-coupled code that utilizes such modeling.[30],[31]

Computational fluid dynamics alone can ultimately achieve limited fidelity in regard to modeling the internal environment of a SRM. To achieve more comprehensive modeling of the total internal ballistics environment, it is necessary to include coupled multi-physics modeling

approaches. Also of importance is capturing the multiphase and multispecies nature of the flow.[32],[33] A fully coupled framework would include a collection of models to capture the true physically of the internal environment, such as boundary-layer models, combustion models, erosive burning models, slag accumulation models, and structural models. These models range from empirical-based models to detailed thermochemistry, aeroacoustic, and solid mechanic theoretics. Erosive burning models typically incorporate empirically determined constants or significant assumptions of the combustion process.[9],[34],[35] Combustion models often have many underlying assumptions due to the unsteady three-dimensional flame structure and numerous chemical species inherent to the combustion process.[36] Slag accumulation is difficult to accurately estimate due to inconsistent quantities reported in literature as well as inconclusive data from recovered motors.[7]

Internal ballistics modeling with CFD provides critical information about a motor and has its place in the design process, however, with today's computational power, highly accurate CFD methods are simply too time consuming for effective use in guiding the overall configurations early in the design process. This brings us closer to the focus of this report, panel methods. These methods are based on potential flow theory, which assumes steady, inviscid, irrotational, and incompressible flow. Panel methods also solve over surface meshes rather than volumetric meshes. These are significant simplifications compared to most CFD solvers, and as such, they require dramatically less computational resource and time. For this reason, they are widely used for preliminary analysis. Despite the simplicity of potential flow assumptions, internal flow solutions based upon potential theory have shown to give exceptional fidelity, such as in the works of Hart and McClure,[18],[19] Saad and Majdalani,[20] Maicke et al.,[21] McClure et al.,[37] Terrill and Colgan,[38] Haloulakos,[39] Majdalani and Saad.[40], and Smith-Kent et al.[41]

1.3 Motivation

The flow in a SRMs combustion chamber is mostly subsonic (excluding nozzleless motors), with most of the flow acceleration occurring in the nozzle. Thus, the internal flow is within the capabilities of a potential-based panel code. FlightStream® is a surface-vorticity solver based on potential flow theory that was originally intended for external flow applications.[42],[43] The objective of this thesis is to demonstrate the viability of FlightStream® for internal flow analysis.

The ability to produce rapid internal flow solutions of medium fidelity with FlightStream® would be immensely advantageous in conceptual and preliminary design processes by allowing numerous designs to be tested in a relatively short amount of time, which is not feasible with higher-order computational models. In the same regard, FlightStream® may prove to be useful as a tool for design optimization. FlightStream® can also be utilized to further develop studies which recognize the inherent coupling between the steady bulk flow and transient fluctuations by addressing them in separate modes. Historically, these analytic solutions, such as those developed by Apte and Yang,[44] Fabignon et al.,[45] Flandro et al.,[46] and Boyer et al.[47] have been limited to simple geometric configurations. FlightStream®'s solution can serve as a basis in such studies allowing for the consideration of much more complex geometries.

2 Internal Flow Solution Method

The following section details how the surface meshes of the SRM models were created as well as the solver methodology of FlightStream®. Most of the modeling can be done internally in FlightStream®, as it features an intuitive user-interface and a CAD module with numerous tools to assist in generating a proper surface mesh.

2.1 Geometry Formulation

FlightStream® offers comprehensive interactivity with modern engineering tools in regard to geometry import. All the models in this report were originally constructed in SOLIDWORKS and imported into FlightStream® as IGES surfaces. The surface meshes represent the exposed surface of the solid propellent grain. Unless the mesh has been fine-tuned prior to importing, it is favorable to import the model as an IGES file rather than a STL file to take advantage of FlightStream®'s CAD module to maximize the geometric integrity of the model. FlightStream® has an assortment of built-in meshing tools to improve raw imported meshes; the trimmed and aligned meshers are particularly helpful in this extent. The trimmed mesher, generally used on irregularly shaped surfaces, generates unstructured isotropic facets. The aligned mesher creates structured anisotropic facets; this is useful on elongated surfaces that require a denser mesh in one dimension than the other, such as the long tubular sections in a solid rocket motor.

It is important to ensure the mesh surface is one continuous structure, otherwise the solver can produce error. FlightStream® has a built-in diagnostic tool as well as a variety of repair tools to fix these meshing errors, should they occur. It is also important to ensure the mesh is of good quality. The solution will be prone to error if the mesh contains facets with extreme aspect ratios. In some instances, it may be beneficial to simplify the model geometry to avoid poor quality meshes.

In FlightStream®, the burning surfaces are declared inlet boundaries. The surface normal specification of the inlet boundary is generally the best option for solid propellant rocket motors, as it will apply a velocity on the surface in the normal direction of each mesh facet. The model should have the surface normals of all mesh faces facing inward. To assist with this, an option can be toggled in FlightStream® to colorize the faces based on the direction of their surface

normals relative to the current scene view. In addition, the surface normals can be flipped rather easily with a built-in toggle. Furthermore, FlightStream® allows an option to specify a custom inlet profile should a variable inlet profile be desired; this is useful for incorporating erosive burn rate augmentation, among other things. This option takes as input a text file of coordinates and corresponding inlet velocities. The specified inlet velocities will be applied to mesh surfaces that are nearest to the corresponding coordinates of the text file. In most cases, it is suitable to define the custom profile down the centerline of the model. This custom inlet feature was added for the purposes of this work and potential future internal flow work with FlightStream®.

2.2 Flow Solver

In FlightStream®, vortex rings are applied to each mesh facet, where each edge is a segmented piece of the vortex. These vortex rings interconnect, sharing edges with neighboring rings and encompassing the entire surface body of the input geometry. The induced velocity is calculated for each segment of these vortex rings according to Biot-Savart's law; that is, based on the plane created by the segment's vertices and the spatial point of induction. The induced velocity of a particular vortex ring is found through summation of the induced velocities of each segment that comprise the ring. The direction of each vortex ring is determined by the facet's normal vector, and as such, facet normals must be configured homogenously. Vortex strength is acquired from known velocities at boundary conditions and abides by Helmholtz's law. To overcome inversion errors of large matrices inherent to large surface meshes, FlightStream® subdivides the mesh and solves each part iteratively. Convergence of the solver is based on the stability of the surface vorticity and wake integration plane.[48],[49],[50]

For the vortex formulation of the potential equations, a freestream velocity must be defined. In the application of internal flows, this freestream velocity is irrelevant (at least for how models

were composed in this study). As such, the freestream velocity was set to a negligibly small value. The definition of the solid rocket motor problem in FlightStream® begins at the fluid flow level. Instead of representing a regressing surface, mesh surfaces represent the inception of gaseous flow. The gaseous injection velocity was calculated through the conservation of mass as the propellant converts from solid to gas.

The surface vortices at the outlet of a SRM model will most often be unbounded. Because of this, the solution becomes unphysical here. In the current work, this was overcome by simply extending the length of models such that the unphysical outlet was beyond the domain being investigated. For all the models tested, smooth convergence was observed and a convergence threshold of 10^{-6} was set as a requirement.

3 Validation Results

Four simple grain geometries were compared to analytical models for validation purposes. Because FlightStream®'s solutions are potential, this work began with irrotational models developed following the work of Majdalani et al., in which the rotational analogs of the presented solutions were derived.[13],[15],[16] A straight cylindrical and straight slab grain are arguably the most basic test cases; these are the first validation cases, accordingly. With insight on these solutions, approximations can be made to the governing equations to find solutions for the other two geometries, a tapered cylindrical and tapered slab grain.

The Space Shuttle Reusable Solid Rocket Motor (RSRM) is a common candidate for validation studies due to its complexity and the abundance of available data on the motor.[30],[31] The RSRM was used to serve as a more complex and realistic validation case. The internal flow of the RSRM is known to be highly rotational and reaches a relatively high Mach number due to the low port-to-throat ratio and high length-to-diameter ratio.[51],[52] Because of this, rotational

and compressible flow corrections are necessary to compare with experimental and other computational results.

3.1 Straight Bore Validation

A solution to the incompressible potential equation was equated and results are given for the straight cylindrical and straight planar geometries. The two-dimensional control volume is identical between the two geometries, however, the difference between the polar and cartesian forms of Laplace's equation results in slightly different analytic solutions. When there is no flow through the headwall, the flow in a planar motor has approximately one-fourth the energy of a cylindrical motor of equivalent dimension. This is of course assuming the flow is predominately in the axial direction, as is typically the case in solid rocket motors.

3.1.1 Cylindrical Model

For completeness and to show the connectivity between rotational and irrotational flow behavior, the analytic solutions to the configurations of interest are repeated here. To begin the derivation, the differential form of the steady-state continuity equation is given in cylindrical coordinates. Axisymmetric and incompressible flow was assumed.

$$\frac{\partial}{\partial \bar{r}}(\bar{\rho}\bar{u}_r\bar{r}) + \frac{\partial}{\partial \bar{\theta}}(\bar{\rho}\bar{u}_\theta) + \bar{r}\frac{\partial}{\partial \bar{z}}(\bar{\rho}\bar{u}_z) = 0 \tag{1}$$

$$\frac{\partial}{\partial \theta} = 0 \qquad \frac{d\bar{\rho}}{d\bar{V}} = 0$$

$$\frac{\bar{u}_r}{\bar{r}} + \frac{\partial \bar{u}_r}{\partial \bar{r}} + \frac{\partial \bar{u}_z}{\partial \bar{z}} = 0 \tag{2}$$

The velocity potential ϕ can be introduced by assuming irrotationality. Substituting this relationship into Eq. (2) results in the well-known Laplace equation in two dimensions.

$$\overline{\nabla} x \vec{u} = 0 \qquad \overline{\nabla}\bar{\phi} = \vec{u} \tag{3}$$

$$\frac{\partial^2 \bar{\phi}}{\partial \bar{r}^2} + \frac{1}{\bar{r}}\frac{\partial \bar{\phi}}{\partial \bar{r}} + \frac{\partial^2 \bar{\phi}}{\partial \bar{z}^2} = 0 \tag{4}$$

A schematic of the control volume of a straight porous tube is shown in Fig. 1. The coordinate system origin was positioned at the central axis of the head end of the motor. The top and bottom walls are slip boundaries that represent the burning surfaces, where the velocity u_b is the burning rate. The aft end is an open boundary, while the head end can be treated as either a homogeneous wall boundary ($u_h = 0$) or a mass injection boundary.

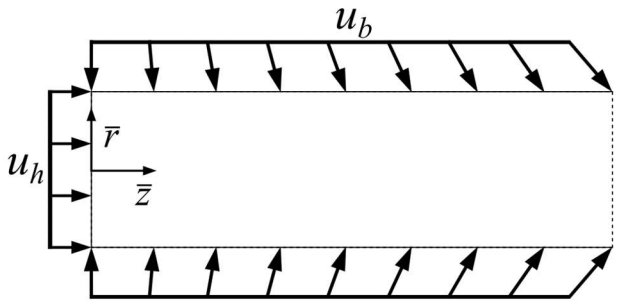

Fig. 1 Control volume of a straight porous chamber.

The boundary conditions are defined as follows:

$$\begin{cases} \lim\limits_{\bar{r}\to 0} \dfrac{\partial \bar{\phi}(\bar{r},\bar{z})}{\partial \bar{r}} = 0 & \text{no flow across centerline} \\ \dfrac{\partial \bar{\phi}(r_b,\bar{z})}{\partial \bar{r}} = -u_b & \text{burning surface injection} \\ \dfrac{\partial \bar{\phi}(\bar{r},0)}{\partial \bar{z}} = u_h & \text{headwall injection} \\ \bar{\phi}(0,0) = 0 & \text{potential flow criterion} \end{cases} :: \tag{5}$$

In going forward, it is practical to normalize the variables and operators by the burning surface radius r_b and the propellant injection velocity u_b as shown below.

$$r = \frac{\bar{r}}{r_b} \qquad z = \frac{\bar{z}}{r_b} \qquad u_r = \frac{\bar{u}_r}{u_b} \qquad u_z = \frac{\bar{u}_z}{u_b} \qquad \nabla = r_b \overline{\nabla} \qquad \phi = \frac{\bar{\phi}}{r_b u_b} \tag{6}$$

The normalized Laplacian retains the same form as seen in Eq. (4) and the boundary conditions simplify to:

$$\frac{\partial^2\phi}{\partial r^2}+\frac{1}{r}\frac{\partial\phi}{\partial r}+\frac{\partial^2\phi}{\partial z^2}=0 \tag{7}$$

$$\begin{cases} \lim\limits_{r\to 0}\dfrac{\partial\phi(r,z)}{\partial r}=0 \\ \dfrac{\partial\phi(1,z)}{\partial r}=-1 \\ \dfrac{\partial\phi(r,0)}{\partial z}=\dfrac{u_h}{u_b}=\beta \\ \phi(0,0)=0 \end{cases} \tag{8}$$

Laplace's equation can be solved rather routinely via the method of separation of variables. The potential function was thus represented as a sum of two intermediate functions.[21]

$$\phi(r,z)=F(r)+G(z) \tag{9}$$

Equation (7) was then separated and integrated, resulting in Eq. (11) and Eq. (12).

$$\frac{\partial^2 F}{\partial r^2}+\frac{1}{r}\frac{\partial F}{\partial r}=-\frac{\partial^2 G}{\partial z^2}=\upsilon \tag{10}$$

$$F(r)=\frac{1}{4}\upsilon r^2+C_1\ln(r)+C_2 \tag{11}$$

$$G(z)=-\frac{1}{2}\upsilon z^2+C_3 z+C_4 \tag{12}$$

The integration constants are thereupon determined with the specified boundary conditions. The result is the potential function for incompressible, irrotational flow in a porous cylindrical chamber where β is the ratio of the headwall velocity to the burning surface velocity.

$$\phi(r,z)=-\frac{r^2}{2}+z^2+\beta z \tag{13}$$

$$u_r=-r \qquad u_z=2z+\beta \tag{14}$$

An interesting characteristic of this solution is that each velocity component is purely one-dimensional. This quality is what allows for the simplification of the governing equations in the

forthcoming models for the tapered geometries. The flow described by Eq. (13) is commonly known as the Hart-McClure profile.[53]

3.1.2 Cylindrical Results

The mesh geometry used in FlightStream® for the tubular model is shown in the figure below. The entire surface was declared an inlet boundary. There are not any constraints on the cylindrical model's dimensions imposed by the analytic model; however, dimensions were chosen such as to represent a typical rocket motor, in which the chamber length is generally much longer than the radius.

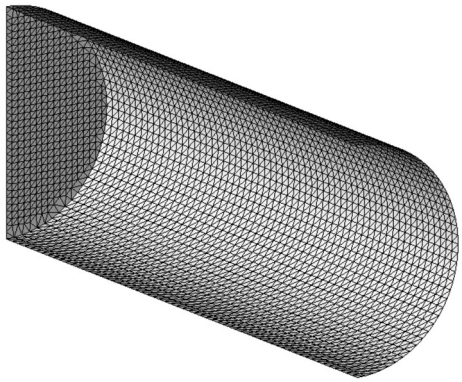

Fig. 2 Straight cylindrical half-model in FlightStream®.

For the first validation case, the headwall velocity was relaxed. A comparison between the nondimensional velocity contours of the analytic model and the FlightStream® results is shown in Fig. 3. The variables are normalized as defined previously in Eq. (6). The flowfields show good agreement except for near the surface boundaries, which was expected. This increase in error is inherent to the surface-vortical approach used by FlightStream®. Near-surface measurements are skewed by the singularities of the vortex rings that comprise the mesh surface. The observed error here is a constituent of post-processing and has no impact on the overall solution. Research in Flight is currently working on a vortex-splitting scheme to attenuate this error.

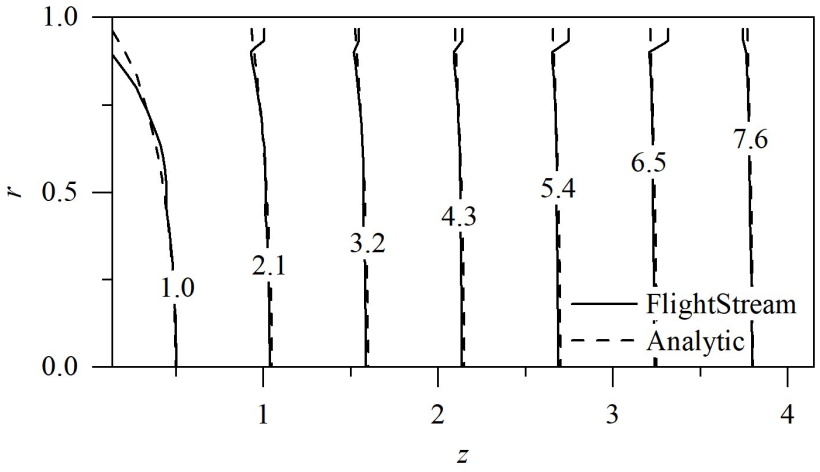

Fig. 3 Velocity contours in the straight cylindrical chamber.

Streamlines are shown in Fig. 4 for the cases of three different headwall injection velocities: no injection, a unit injection ratio, and an injection ratio of 5. Streamlines were generated using OriginPro plotting software. This program features a graphing function that generates streamlines from an input velocity field matrix. The velocity fields of the analytic solution and FlightStream®'s solution were loaded into Origin, and the stream-field densities were set to equal values. The slip condition can be observed in the streamlines; further down the axis of the chamber, the flow enters from the burning surface evermore tangentially. This is distinctly different from the rotational solution, in which the flow is required to enter perpendicular to the burning surface throughout the entire domain. The headwall velocity is essentially just a flow constant, as seen in Eq. (14), that linearly adds to the magnitude of the axial velocity. Increasing the headwall velocity increases the relative strength of the mean flow; this can be seen in the streamline plots. The analytic model and FlightStream®'s results agree well for all three cases.

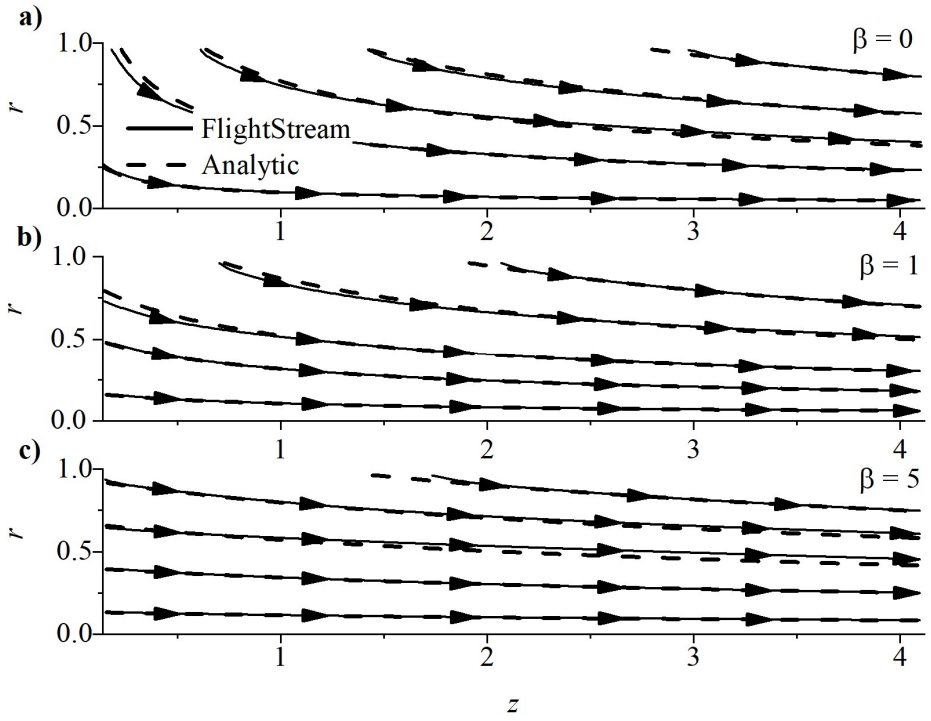

Fig. 4 Streamlines in the straight cylindrical chamber for three headwall injection velocities.

3.1.3 Planar Model

A solution of similar form was derived for the case of a planar motor following the same method as the cylindrical case. Laplace's equation now, however, takes the cartesian form, where instead of axisymmetry, no crossflow was assumed ($\frac{\partial}{\partial \bar{z}} = 0$).

$$\frac{\partial^2 \phi}{\partial x^2} + \frac{\partial^2 \phi}{\partial y^2} = 0 \tag{15}$$

The control volume shown in Fig. 1 can just as fittingly represent the slab motor, where the abscissa is represented by *x* instead of *z*, the ordinate is represented by *y* instead of *r,* and the boundary conditions were transformed accordingly.

$$\begin{cases} \lim\limits_{y\to 0}\dfrac{\partial\phi(x,y)}{\partial y}=0 \\ \dfrac{\partial\phi(x,1)}{\partial y}=-1 \\ \dfrac{\partial\phi(0,y)}{\partial x}=\dfrac{u_h}{u_b}=\beta \\ \phi(0,0)=0 \end{cases} \tag{16}$$

Carrying forth with separation of variables just as previously, the incompressible potential solution for the slab motor is written as

$$\phi(x,y) = -\frac{y^2}{2}+\frac{x^2}{2}+\beta x \tag{17}$$

$$u_y=-y \qquad u_x=x+\beta \tag{18}$$

This solution is nearly identical to Eq. (13) found for the cylindrical motor but has slight modification to the axial velocity. When the headwall injection is relaxed, the flowfield in a planar motor is approximately half the strength of the flowfield in a cylindrical motor of similar scale.

3.1.4 Planar Results

The mesh geometry for the planar motor is shown in Fig. 5. Unlike for the cylindrical case in which the dimensions could be chosen rather freely, the slab motor model must be sufficiently wide such that the inert side walls do not affect the desired two-dimensional flowfield.

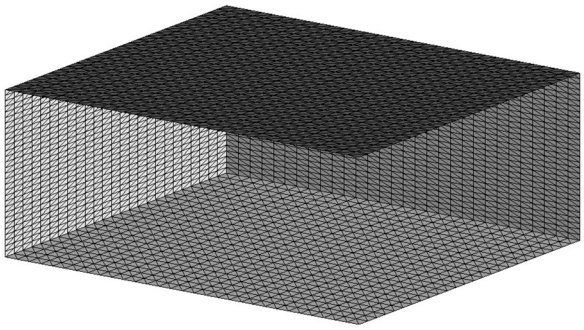

Fig. 5 Straight planar half-model in FlightStream®.

The nondimensional velocity contours are shown below for the FlightStream® results and the analytic model for the case of no headwall injection. There is a bit more curvature to the contour lines of the flow in the planar model than that of the cylindrical model. This is attributed to the radial velocity being more dominant in the total flow magnitude than in the cylindrical parallel.

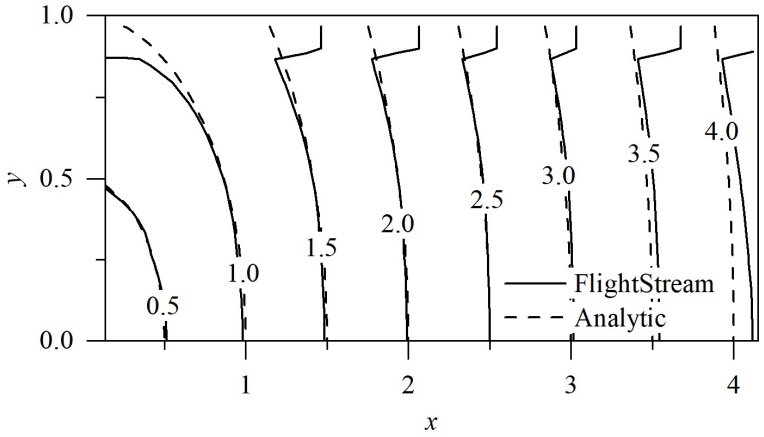

Fig. 6 Velocity contours in the straight planar chamber.

The FlightStream® results and analytic model agree well, however, the FlightStream® solution begins to slightly lag the analytic solution as the axial distance from the headwall increases. For the same reason as before, there was expected error near the mesh surface. The streamlines (generated with OriginPro, as before) are shown in Fig. 7 for the slab motor with and without headwall injection. Again, there was very nice agreement between FlightStream® and the analytic model for all the tested cases. Interestingly, the streamlines do not appear to be affected by the error along the centerline observed in Fig. 6.

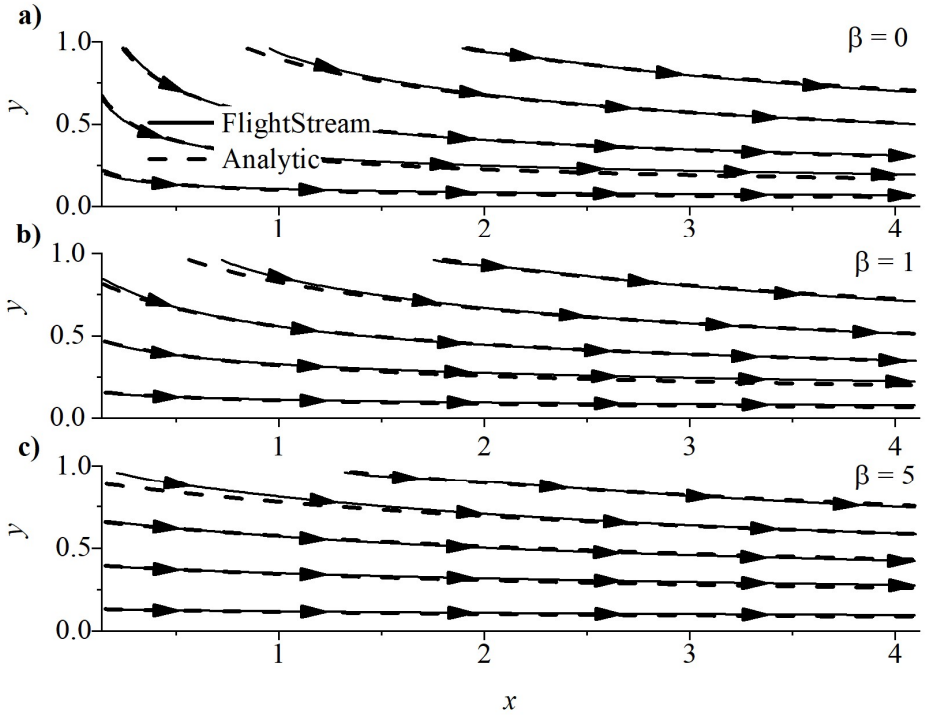

Fig. 7 Streamlines in the straight planar chamber for three headwall injection velocities.

3.2 Tapered Bore Validation

The stream function was used to find an analytic solution for the tapered cylindrical and tapered slab geometries. The model assumes that the taper angle is small, which imposes a limit on the geometry that can be accurately validated with this model. Thus, the analyses were restricted to low taper angles. It is shown that even small taper angles can have a considerable effect on the flowfield. There are also limits exacted by mass conservation due to the increasing area of the chamber that must be respected. The solutions found here are identical to the two previous geometries when the taper angle is set to zero.

3.2.1 Cylindrical Model

With the addition of a taper angle, the incompressible potential function can no longer be solved in the same manner as previous analyses. The nonhomogeneous (burning surface injection) boundary that determines the separation constant in the method of separation of

variables is now a function of the axial distance, and thus a separated "constant" cannot be determined. Stokes stream function is useful in this case, as small angle approximations can be made to reduce the equation of motion to an ordinary differential equation; a similar procedure is outlined by Sams & Majdalani for rotational flow.[15],[16] The stream function is defined for axisymmetric incompressible flow such that continuity is guaranteed to be satisfied; the polar forms are shown below.

$$\bar{u}_r = -\frac{1}{r}\frac{\partial \bar{\Psi}}{\partial \bar{z}} \qquad \bar{u}_z = \frac{1}{r}\frac{\partial \bar{\Psi}}{\partial \bar{r}} \tag{19}$$

By setting the velocity curl equal to zero and substituting Eq. (19) into the equation, the stream function for irrotational flow is realized.

$$\overline{\nabla} x \vec{u} = 0 \tag{20}$$

$$\frac{\partial^2 \bar{\Psi}}{\partial \bar{r}^2} - \frac{1}{\bar{r}}\frac{\partial \bar{\Psi}}{\partial \bar{r}} + \frac{\partial^2 \bar{\Psi}}{\partial \bar{z}^2} = 0 \tag{21}$$

The variables and operators were normalized as before, however now the radius varies throughout the chamber. Thus, the radius of the burn surface at the head of the chamber r_0 was used for normalization.

$$\overline{r_b}(\bar{z}) = r_0 + \bar{z} tan\alpha \tag{22}$$

$$r = \frac{\bar{r}}{r_0} \qquad z = \frac{\bar{z}}{r_0} \qquad u_r = \frac{\bar{u}_r}{u_b} \qquad u_z = \frac{\bar{u}_z}{u_b} \qquad \nabla = r_0 \overline{\nabla} \qquad \Psi = \frac{\bar{\Psi}}{r_0 u_b} \tag{23}$$

The control volume for the tapered grain geometry is shown in Fig. 8 with the normalized boundary conditions given beneath. The setup is the same as shown previously for the straight chamber, but with the addition of a taper angle α along the burning surface.

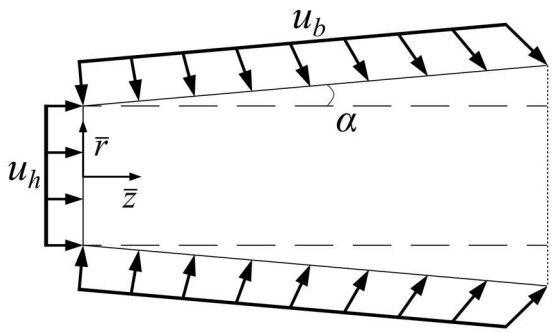

Fig. 8 Control volume of a tapered porous chamber.

$$\begin{cases} u_r(r_b, z) = -cos\alpha \\ \qquad\qquad\qquad\qquad \text{burning surface injection} \\ u_z(r_b, z) = sin\alpha \\ \qquad\qquad\qquad\qquad :: \\ u_r(0, z) = 0 \qquad \text{no flow across centerline} \\ u_z(r, 0) = \beta \qquad \text{headwall injection} \end{cases} \tag{24}$$

Referring back to the solution for a straight cylinder, the radial velocity was shown to vary only in the radial direction. Therefore, it is reasonable to assume for small taper angles that the radial velocity will have a negligible dependance on the axial position; in doing so, Eq. (21) is reduced to an ordinary differential equation.

$$\frac{\partial u_r}{\partial z} = \frac{1}{r}\frac{\partial^2 \Psi}{\partial z^2} \approx 0 \tag{25}$$

$$\frac{\partial^2 \Psi}{\partial r^2} - \frac{1}{r}\frac{\partial \Psi}{\partial r} = 0 \tag{26}$$

The stream function at the burning surface must be determined to bound and solve Eq. (26). This was conducted in the same manner as Refs. [15] and [16]. Below are definitions for the burning surface radius r_b and axial distance z in terms of the tapered surface s and the normalized velocity components at the burning surface.

$$u_r(r_b, z) = -\frac{1}{r}\frac{\partial \Psi_b}{\partial z} = -cos\alpha \tag{27}$$

$$u_z(r_b, z) = \frac{1}{r}\frac{\partial \Psi_b}{\partial r} = sin\alpha \tag{28}$$

$$z = scos\alpha \tag{29}$$

$$r_b = 1 + ztan\alpha = 1 + ssin\alpha \tag{30}$$

Using these four equations, the derivative of the stream function along the burning surface was found to simply be the burning surface radius, Eq. (30).

$$\frac{d\Psi_b}{ds} = \frac{\partial \Psi_b}{\partial r}\frac{dr}{ds} + \frac{\partial \Psi_b}{\partial z}\frac{dz}{ds} = r_b \tag{31}$$

Integrating Eq. (31) and substituting Eq. (29) into the expression yields the stream function along the burning surface as a function of *z*.

$$\Psi_b(s) = s + \tfrac{1}{2}s^2 sin\alpha + C \tag{32}$$

$$\Psi_b(z) = zsec\alpha\left(1 + \frac{1}{2}ztan\alpha\right) + C \tag{33}$$

To determine the integration constant, the headwall boundary condition was integrated and evaluated at the burning surface.

$$\int u_z(r, 0)\Big|_{r=1} = \frac{1}{r}\frac{\partial \Psi_b(0)}{\partial r} = \beta \tag{34}$$

$$\Psi_b(0) = \left(\frac{\beta}{2}r^2 + C\right)\Big|_{r=1} \tag{35}$$

The integration constant in Eq. (35) can be set to zero in accordance with the definition of the stream function, and thus, the stream boundary condition along the burning surface is determined.

$$\Psi_b(0) = \frac{\beta}{2} \tag{36}$$

$$\Psi_b(z) = zsec\alpha\left(1 + \frac{1}{2}ztan\alpha\right) + \frac{\beta}{2} \tag{37}$$

With this, the problem is fully defined as:

$$\frac{\partial^2 \Psi}{\partial r^2} - \frac{1}{r}\frac{\partial \Psi}{\partial r} = 0 \tag{38}$$

$$\Psi(0, z) = 0 \qquad \Psi(r_b, z) = \Psi_b \tag{39}$$

The solution was then determined with simple integration.

$$\Psi(r, z) = \left[z sec\alpha \left(1 + \frac{1}{2} z tan\alpha\right) + \frac{\beta}{2} \right] \frac{r^2}{{r_b}^2} \tag{40}$$

It is important to note the flow limitations imposed by mass conservation in a tapered chamber. Unlike a straight chamber in which the velocity continuously increases down the length of the motor, the velocity field in a sufficently long tapered chamber will converge to a constant value;[15],[16] this is demonstrated with the following analysis, which was slightly modified from the referenced reports to account for the differences between the analytical setups.

The normalized headwall area, burning surface area, and outflow area, represented as A_h, A_b, and A_e, respectfully, are defined below.

$$A_h = \pi \tag{41}$$

$$A_b(z) = 2\pi z sec\alpha \left(1 + \frac{1}{2} z tan\alpha\right) \tag{42}$$

$$A_e(z) = \pi(1 + z tan\alpha)^2 \tag{43}$$

The bulk flow velocity u_{avg} as a function of axial distance z was determined by applying continuity.

$$u_{avg}(z) A_e(z) = \beta A_h + A_b \tag{44}$$

$$u_{avg}(z) = \frac{\beta + 2 z sec\alpha \left(1 + \frac{1}{2} z tan\alpha\right)}{(1 + z tan\alpha)^2} \tag{45}$$

By dividing Eq. (45) by z, the velocity limit as z approaches infinity is easily realized.

$$u_{avg}(z) = \frac{\frac{\beta}{z} + 2sec\alpha(\frac{1}{z} + \frac{1}{2}tan\alpha)}{(\frac{1}{z} + tan\alpha)^2} \tag{46}$$

$$\lim_{z\to\infty} u_{avg}(z) = csc\alpha \tag{47}$$

The velocity in a tapered section must always be less than or equal to this limiting value in order for continuity to be satisfied. For this reason, the headwall injection velocity must respect this limit to ensure a valid solution.

$$\beta \leq u_{avg}(\infty) \tag{48}$$

$$\beta \leq csc\alpha \tag{49}$$

Because the analytic model assumes small taper angles, a small angle approximation is appropriate here.

$$\beta \leq \frac{1}{\alpha} \tag{50}$$

Consider the case of a maximum small angle of 5 degrees. The headwall injection velocity ratio in this case is therein

$$\beta \leq \frac{36}{\pi} \approx 11.46 \tag{51}$$

3.2.2 Cylindrical Results

The mesh geometry for the cylindrical model with a taper angle of 2 degrees is shown in Fig. 9. Dimensions were chosen as to be consistant with the previous analysis. The headwall injection velocities now have an upper limit prescribed by continuity; the cases tested were well within this limit.

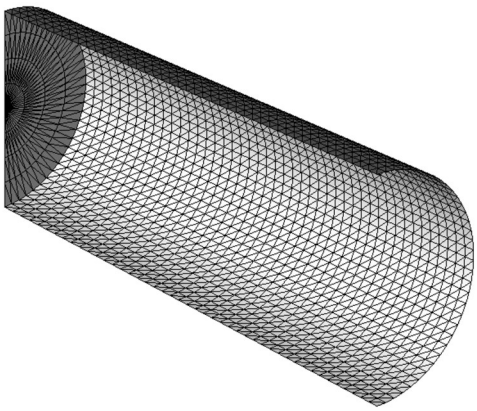

Fig. 9 2-degree tapered cylindrical half-model in FlightStream®.

The nondimensional velocity contours are presented in the figure below. Notice the velocity magnitude is slightly lower than the straight-chambered counterpart due to the increasing area of the chamber. FlightStream® and the analytic model show good agreement throughout the entire domain. The expected errors at the burning surface appear to diminish in magnitude as the flow develops; this could just be a facet of this particular solution, as a slight taper really shouldn't have an effect on the error in this region. Nevertheless, it is interesting to observe in the results.

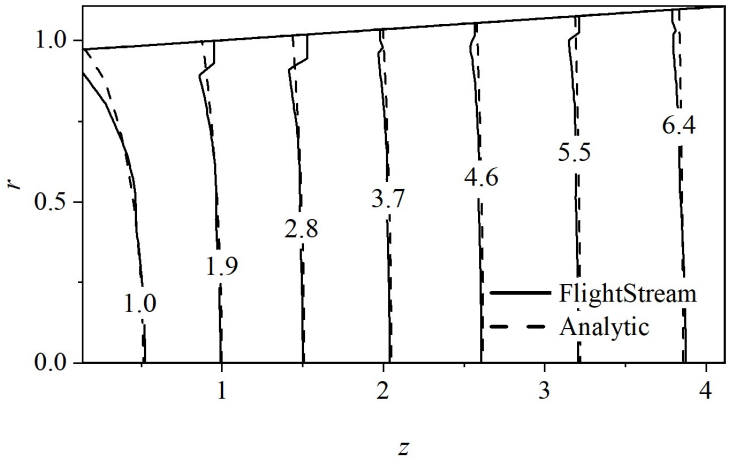

Fig. 10 Velocity contours in the 2-degree tapered cylindrical chamber.

The streamlines for the headwall injection cases are generally in good agreement. For the case of no headwall injection, the two solutions are nearly indistinguishable. For the two cases with mass injection through the headwall, there are localized departures from the nice alignment

between the two models; this must be due to some difference between the flowfields. The offset streamlines, however, remain non-intersecting and appear parallel. The streamlines near the centerline are nearly indistinguishable for all three of the cases investigated.

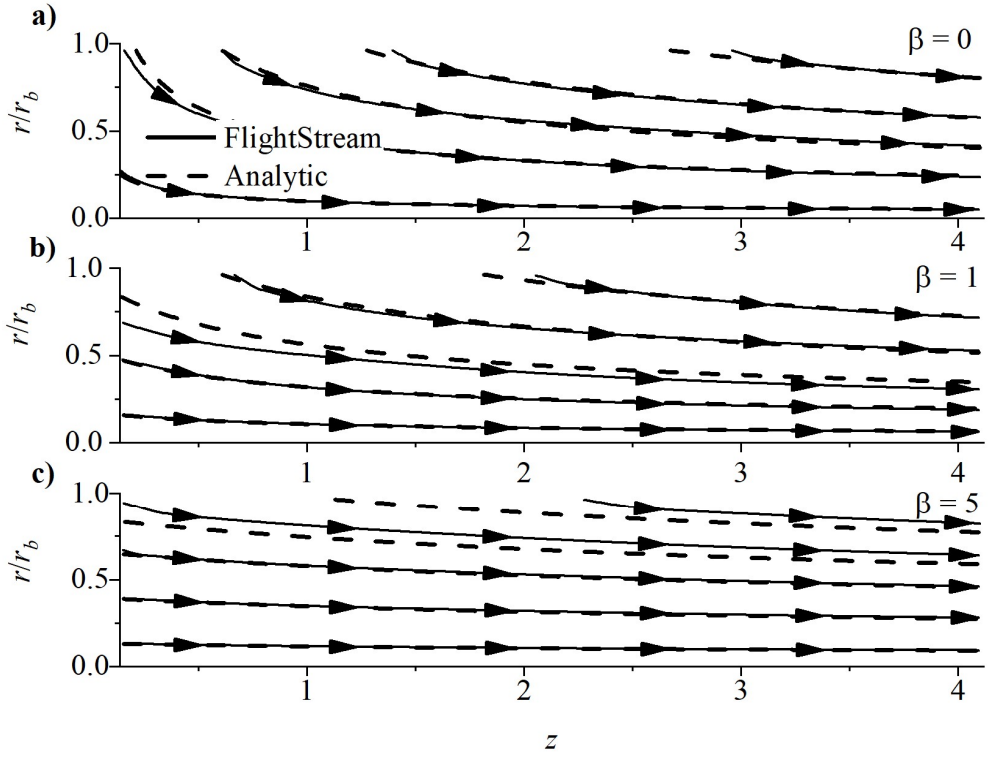

Fig. 11 Streamlines in the 2-degree tapered cylindrical chamber for three headwall injection velocities.

Bernoulli's equation can be used to relate the flow properties between any two points in the chamber, given the flow is irrotational. This relation was used to compute the change in pressure along the centerline of the tapered geometries. The reference point was taken to be the burning surface inlet condition and the change in pressure was normalized by the burning surface dynamic pressure q_b.

$$\frac{\Delta P(z)}{q_b} = 1 - \frac{u(0,z)^2}{{u_b}^2} \tag{52}$$

The axial pressure profiles are shown in Fig. 12 for taper angles ranging from 0 to 3 degrees. FlightStream® and the analytic model produce essentially identical results.

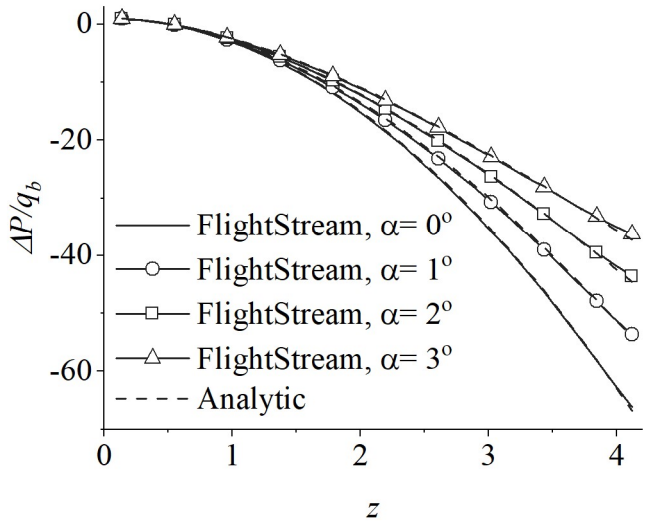

Fig. 12 Pressure coefficient profiles for the cylindrical chambers.

3.2.3 Planar Model

As before, the same problem can be reframed for a tapered slab motor with cartesian coordinates.[15],[16] Instead of axisymmetric flow, no crossflow was assumed. The control volume shown in Fig. 8 remains the same, where now the abscissa is represented by *x* and the ordinate by *y*. The normalized boundary conditions are rewritten as:

$$\begin{cases} u_y(x, y_b) = -cos\alpha \\ u_x(x, y_b) = sin\alpha \\ u_y(x, 0) = 0 \\ u_x(0, y) = \beta \end{cases} \tag{53}$$

After making the same small angle approximation as in the cylindrical analyses, the governing equation in cartesian form reduces to:

$$\frac{\partial^2 \Psi}{\partial y^2} = 0 \tag{54}$$

The stream function along the burning surface assumes a different form than the cylindrical case due to the different relationships between the polar and cartesian definitions of the stream function, shown in Eq. (55) and Eq. (56).

$$u_y(x, y_b) = -\frac{\partial \Psi_b}{\partial x} = -cos\alpha \tag{55}$$

$$u_x(x, y_b) = \frac{\partial \Psi_b}{\partial y} = sin\alpha \tag{56}$$

$$x = scos\alpha \tag{57}$$

$$y_b = 1 + xtan\alpha = 1 + ssin\alpha \tag{58}$$

The stream function along the burning surface was determined in the same manner as before;[15],[16] the four equations above are used in Eq. (59). Integrating this equation and substituting in Eq. (57) gives the stream function boundary condition along the burning surface as a function of *x*.

$$\frac{d\Psi_b}{ds} = \frac{\partial \Psi_b}{\partial y}\frac{dy}{ds} + \frac{\partial \Psi_b}{\partial x}\frac{dx}{ds} = 1 \tag{59}$$

$$\Psi_b(x) = xsec\alpha + C \tag{60}$$

The integration constant was determined using the headwall boundary condition. The integration constant in Eq. (62) was set to zero, as in the cylindrical case.

$$\int u_x(0, y)\Big|_{y=1} = \frac{\partial \Psi_b(0)}{\partial y} = \beta \tag{61}$$

$$\Psi_b(0) = (\beta y + C)|_{y=1} \tag{62}$$

$$\Psi_b(0) = \beta \tag{63}$$

The other boundary condition is the same homogeneous condition along the centerline as the cylindrical analysis. The stream function was then determined by integrating Eq. (54).

$$\Psi(x,y) = [x sec\alpha + \beta]\frac{y}{y_b} \tag{64}$$

As in the cylindrical case, continuity must be respected when applying a headwall injection velocity. The normalized headwall area, burning surface area, and outflow area, represented as A_h, A_b, and A_e, respectfully, are defined below.

$$A_h = 2w \tag{65}$$

$$A_b(x) = 2w * x sec\alpha \tag{66}$$

$$A_e(x) = 2w(1 + x tan\alpha) \tag{67}$$

The bulk flow velocity u_{avg} as a function of axial distance x was determined by applying continuity.

$$u_{avg}(x)A_e(x) = \beta A_h + A_b \tag{68}$$

$$u_{avg}(x) = \frac{\beta + x sec\alpha}{1 + x tan\alpha} \tag{69}$$

Once again, the velocity limit as x approaches infinity was determined. As it turns out, the planar model has the same restiction imposed on the headwall injection velocity as the cylindrical case of analogous boundary conditions.

$$u_{avg}(x) = \frac{\frac{\beta}{x} + sec\alpha}{\frac{1}{x} + tan\alpha} \tag{70}$$

$$\lim_{x\to\infty} u_{avg}(x) = csc\alpha \tag{71}$$

$$\beta \leq csc\alpha \approx \tfrac{1}{\alpha} \tag{72}$$

3.2.4 Planar Results

The FlightStream® geometry for the tapered slab with a two-degree taper angle is shown in Fig. 13. As with the straight planar model, the side walls were set sufficiently far apart such that the desired two-dimensional flowfield was unimpeded.

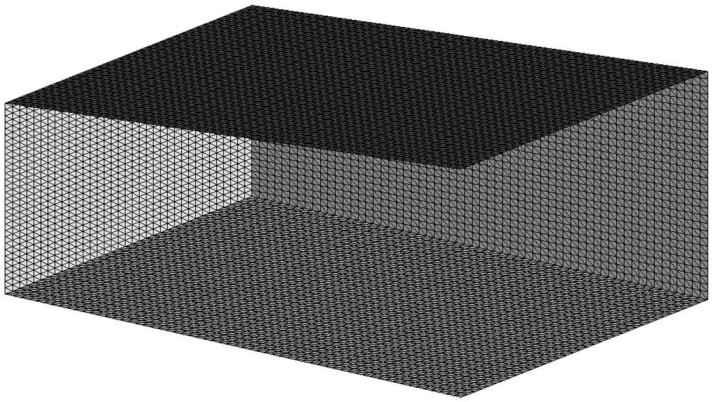

Fig. 13 2-degree tapered planar half-model in FlightStream®.

The nondimensional velocity contours for the two-degree tapered slab are presented in Fig. 14. There is good agreement between FlightStream® and the analytical model, but just as with the previous planar model, the velocity field found with FlightStream® slightly lags the analytical solution as the axial distance increases. The greatest error is seen to occur near the centerline, excluding the expected error near the burning surface boundary.

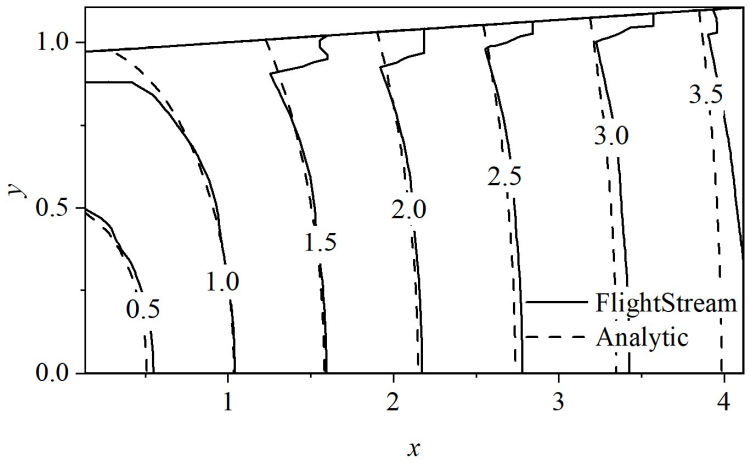

Fig. 14 Velocity contours in the 2-degree tapered planar chamber.

Despite this error, the streamlines generated with OriginPro for the three headwall injection cases again show good correspondence throughout the entire domain. The localized differences observed in the tapered cylindrical motors streamlines (Fig. 11) are not seen in the planar results.

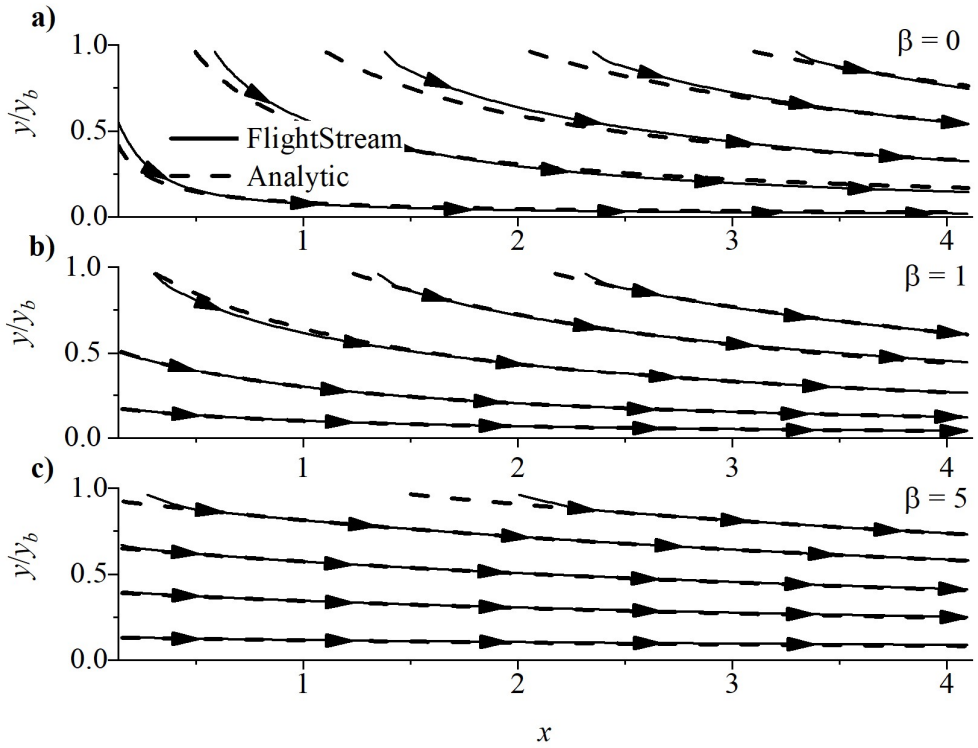

Fig. 15 Streamlines in the 2-degree tapered planar chamber for three headwall injection velocities.

Bernoulli's equation was used as before (Eq. (52)) to determine the centerline pressure profiles for a range of taper angles. The results are compared with the analytical model in Fig. 16. There is a uniform discrepancy between the two solutions near the end of the chamber for all the taper angles tested; this coincides with the error observed in Fig. 14. Because the error does not appear to be a function of the taper angle, it can be attributed to an issue shared between both the straight and tapered planar geometries. It is possible that the finite width of the model in FlightStream® is causing the deviation from the analytic model.

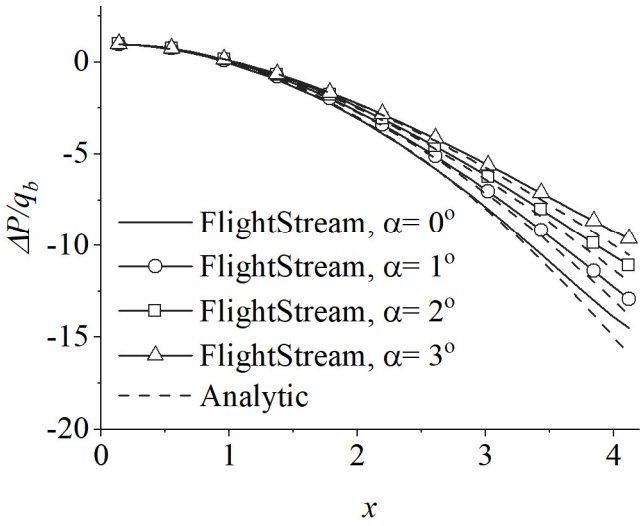

Fig. 16 Pressure coefficient profiles for the planar chambers.

3.3 RSRM Validation

The following section covers the validation study conducted on the Space Shuttle Reusable Solid Rocket Motor (RSRM). The RSRM's propellant properties and geometry were obtained from Thiokol's design proposal.[54] Being a tangible motor, there are many complex processes that influence the internal flowfield, as outlined in the introduction of this paper. To better compare with the validation data, two corrections are applied to FlightStream®'s results: a rotational correction and a compressibility correction. Both corrections are based on the Taylor-Culick profile.

3.3.1 RSRM Model

The RSRM model was developed as to represent the steady-state flow just after ignition transients assuming negligible change to the initial grain geometry. A CAD surface of the half-model was created using SOLIDWORKS and imported into FlightStream® as an IGES file; this surface is shown in Fig. 17.

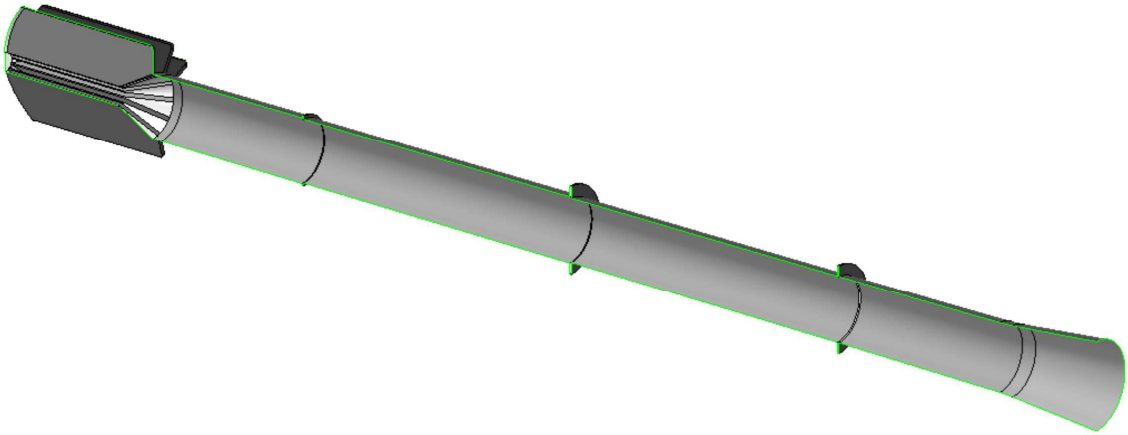

Fig. 17 RSRM half-model in FlightStream®.

The RSRM consists of four segments: a forward finocyl section, two central sections with slight taper (less than 1 degree), and a tapered aft section. The forward section has 11 fins that port into the central cylindrical chamber. The slots between each motor segment are inhibited on the aft sides. Thus, in FlightStream® they are left as non-inlet surfaces. These slots have a more dominate influence in rotational flow than in the irrotational flow solution, where they are essentially just thin regions of increased mass flow at the burning surface; this disparity is observed in the following results and is arguably the main source of error. The aft section has a larger taper that widens further near the outlet to allow the nozzle to sit inside. The resultant cavity between the submerged nozzle and the burning surface generates a pocket of recirculating flow; this region and the nozzle were not included in the model. Besides the inhibitors, the entire surface of the RSRM model was declared an inlet boundary in FlightStream®.

The propellent properties obtained from Thiokol's design proposal[54] are shown in Table 1. The gas was assumed to be calorically perfect. The speed of sound a_0 was calculated using the propellent flame temperature T_f.

$$a_0 = \sqrt{\gamma R T_f} \tag{73}$$

Table 1 RSRM propellant properties.

Propellent density, ρ_p	0.0702	lb/in^3
Molar weight	28.5	lb/lb-mol
Flame temperature, T_f	5720	^{o}F
Pressure exponent, n	0.35	
Temperature coefficient, a	0.0364	(in/s)*(psi)$^{-n}$
Specific heat ratio, γ	1.14	

The chamber pressure was taken to be 900 psi. The solid-fuel regression rate δ was determined using the empirical burning rate equation, Eq. (74). Using conservation of mass, a relation between the regression rate and the injection velocity along the burning surface u_b was determined. The solid propellent density is represented by ρ_p and the gaseous density is represented by ρ_g.

$$\delta = aP^n \tag{74}$$

$$u_b = \frac{\rho_p \delta}{\rho_g} \tag{75}$$

Table 2 RSRM flow properties.

Headend Pressure, P	900	psi
Speed of sound, a_o	3505	ft/s
Regression rate, δ	0.394	in/s
Gas density, ρ_g	2.24x10^{-4}	lb/in^3
Gas injection velocity, u_b	123.4	in/s

The finalized mesh in FlightStream® consists of approximately 28,500 faces; a close view of the mesh is shown in Fig.18. A slight simplification of the geometry was necessary to improve the quality of the mesh at the outlet of the finocyl section. The fillets on the aft portion of the fins were removed to allow for the use of the aligned mesher on the central triangular faces. This change has a minor impact on the overall flowfield but was found to be necessary to ensure an accurate solution in this region.

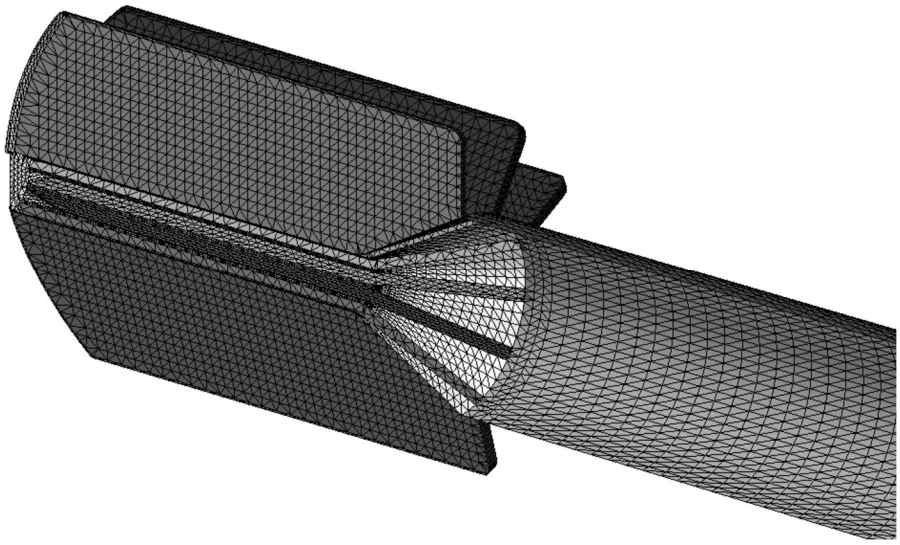

Fig. 18 RSRM mesh in FlightStream®.

3.3.2 Rotational Flow Correction

The internal flowfield of the RSRM is known to be highly rotational as a result of the propellant mass injection as well as the radial slots between the motor segments.[51],[52] Vortex shedding occurs at these slots with oscillatory amplitudes similar in magnitude to the internal acoustic waves. Recirculation occurs aft of the inhibitor slots along the burning surface.[4] As the grain regresses, the inhibitors protrude further into the mean flow. The resulting pressure gradient causes the inhibitors to flex and oscillate, inducing perturbations in the pressure and vortex shedding frequency; this is believed to be a driving force of instabilities.[55] This transient

behavior is currently disregarded in the steady-state formulation presented here. Nevertheless, it is beneficial to be aware of these processes, as they may have some influence on experimental data. Future works may seek to utilize a perturbation-based model to couple the transient flow to the steady solution. The current work focuses on the steady solution for the determination of the static pressure profile. Although a rotational correction was applied to FlightStream®, the recirculating regions aft of the grain slots were not captured by this method, and thus, there was expected error.

A spectrum of energy states has been revealed by Saad and Majdalani linking the purely potential Hart-McClure profile to the Taylor-Culick and beyond to greater energetic states.[20] The irrotational solution (FlightStream®'s solution) was found to represent the minimum kinetic energy state, as predicted by Kelvin's minimum energy theorem. The steady-state internal flow is best represented by the Taylor-Culick profile, which was shown to be an equilibrium state, entailing the most entropy in this energy spectrum. The initiation of the internal flow is likely to be irrotational, as there is little vorticity present. As vorticity is generated at the wall due to the injection process, the flow presumably develops until it reaches maximum entropy intrinsic to the Taylor-Culick profile.

In deriving the Taylor-Culick profile, the stream function (Eq. 13) is substituted into the vorticity transport equation for steady inviscid flow. The variables are normalized in the same manner as the previous analyses.

$$r = \frac{\bar{r}}{r_b} \qquad z = \frac{\bar{z}}{r_b} \qquad u_r = \frac{\bar{u}_r}{u_b} \qquad u_z = \frac{\bar{u}_z}{u_b} \qquad \nabla = r_b\overline{\nabla} \qquad \Psi = \frac{\bar{\Psi}}{r_b u_b} \qquad \Omega = \frac{\bar{\Omega} r_b}{u_b} \tag{76}$$

$$\nabla x(\vec{u} x \Omega) = 0 \qquad \Omega = \nabla x \vec{u} \tag{77}$$

$$\frac{\partial^2 \bar{\Psi}}{\partial \bar{r}^2} - \frac{1}{\bar{r}}\frac{\partial \bar{\Psi}}{\partial \bar{r}} + \frac{\partial^2 \bar{\Psi}}{\partial \bar{z}^2} = -r\Omega = -r^2 f(\Psi) \tag{78}$$

The boundary conditions are the same as in the irrotational model, however no headwall velocity was considered and now the no-slip condition is imposed on the burning surface.

$$\begin{cases} u_r(0,z) = 0 \\ u_r(1,z) = -1 \\ u_z(1,z) = 0 \\ u_z(r,0) = 0 \end{cases} \tag{79}$$

With these conditions, the solution to Eq. (78) is determined.[12]

$$\Psi = z sin\left(\frac{\pi}{2} r^2\right) \tag{80}$$

The Taylor-Culick profile has been extended to cases of the tapered cylindrical and planar motors in the works of Sams et al.[15],[16] These solutions are presented below: the tapered cylindrical, straight planar, and tapered planar stream functions are given as Eq. (81), Eq. (82), and Eq. (83), respectfully.

$$\Psi = z sec\alpha \left(1 + \frac{1}{2} z tan\alpha\right) sin\left(\frac{\pi}{2} \frac{r^2}{{r_b}^2}\right) \tag{81}$$

$$\Psi = x sin\left(\frac{\pi}{2} y\right) \tag{82}$$

$$\Psi = (x sec\alpha) \frac{y}{y_b} \tag{83}$$

In both the irrotational and rotational solutions, the radial velocity approaches zero at the centerline. For the flow fields described in the previous validation cases and in Eqs. (80)-(83), all the axial velocities are linearly dependent on the axial distance. Therefore, a linear relationship can be determined between the irrotational (FlightStream®) and the rotational models. Along the centerline, that relationship is as follows:

$$(u_r)_{ROT} = (u_r)_{FS} = 0 \tag{84}$$

$$(u_z)_{ROT} = \frac{\pi}{2}(u_z)_{FS} \tag{85}$$

From this exercise, it can be deduced that by multiplying FlightStream®'s centerline velocity by $\pi/2$ the exact rotational velocity along the centerline is recovered. This result is obtained regardless of whether there is headwall injection or not, due to the linearity with respect to the axial distance. Equation (85) is simply the relation between the maximum rotational velocity and the average bulk velocity. The aft section of the RSRM is entirely composed of tapered cylindrical segments, thus Eq. (84) and Eq. (85) can represent the rotational flow along centerline with high accuracy aft of the finocyl section in the RSRM (in the absence of recirculation). The region that potentially deviates from this simple conversion is the central bore of the finocyl segment. Here the flow will be three-dimensional, as the flow injects into the bore from the fin slots. In fact, it was found that the irrotational solution is more accurate in the finocyl section than applying this correction.

In a rotational flow, the no-slip condition is upheld along the burning surface. The injection Mach numbers in a SRM are relatively small compared to the flow through the chamber, and the flow near the wall can be considered nearly stagnant. This results in a stagnation pressure loss along the burning surface. The gas propellant regression rate and gas injection velocity are both functions of pressure. As such, the injection velocity will increase as the total pressure drops along the burning surface. In this analysis, it was found that the injection velocity increases by nearly 10% toward the rear of the RSRM. To account for this, this effect was "coupled" to the FlightStream® solution iteratively with the use of the custom inlet profile. First an initial solution was found with constant injection velocity throughout the entire chamber. With this solution, the centerline static pressure was calculated assuming isentropic flow along the centerline.

$$P = P_0(1 + \frac{\gamma - 1}{2} M^2)^{\frac{-\gamma}{\gamma - 1}} \tag{86}$$

At a given axial location, the pressure of the injecting fluid at the burning surface was assumed to be approximately equal to the static pressure at the centerline. With this pressure profile, the new regression rates, injecting gas densities, and gas injection velocities are calculated with Eq. (74) and Eq. (75). This custom inlet profile was then fed back into FlightStream® and a more accurate solution was obtained. In doing this, the solution converged rather quickly, typically by two or three of these iterations.

3.3.3 Compressibility Correction

Due to the high length-to-diameter and low port-to-throat ratio, the flow in the combustion chamber reaches relatively high Mach numbers. Upon applying the rotational correction, it was evident that compressibility effects are not negligible. To account for this, the compressible Taylor-Culick profile derived by Majdalani was used.[14] The derivation is based on perturbation theory and is particularly useful as the first order compressibility correction can simply be amended to FlightStream®'s solution (after applying the rotational correction).

$$(u_z)_{corrected} = \frac{\pi}{2}(u_z)_{FS} + \zeta_{comp} \tag{87}$$

$$\zeta_{comp} = {M_w}^2 \frac{\pi}{96}(u_z)_{FS} \left\{ 8\pi^2 \left[\left(\frac{z - z_0}{R_{avg}} \right) + \frac{\beta}{\pi} \right]^2 - 23\pi + 34.41 \right\} \tag{88}$$

It is important to note that this correction was derived for a non-tapered cylindrical chamber with constant injection velocity. The correction was applied just aft of the finocyl section, when the nearly straight cylindrical chamber of the RSRM begins. The correction was shifted to account for the "headwall" velocity (flow coming from the finocyl) at this starting point; the axial distance was shifted by the starting location z_0 at the outlet of the finocyl and the "headwall" velocity ratio is represented by β. The average radius of the two central motor

segments R_{avg} was used. The taper on the aft section and the variable inlet velocity of the RSRM means that there will inevitably be error in using this compressibility correction. However, the correction is of the first order, so the error caused by this was assumed to be negligible.

3.3.4 RSRM Results

To begin, a comparison between one-dimensional flow and FlightStream®'s solution without correction was made. The axial velocity of the irrotational solution is nonvariant in the radial direction, at least for the previously tested geometries. Considering the RSRM is mostly comprised of a combination of those geometries, there should be good agreeance between FlightStream®'s solution and one-dimensional flow. The one-dimensional velocity was calculated using conservation of mass at discrete axial locations throughout the motor.

$$u(z) = \frac{A_{in}(z) * u_b}{A_{out}(z)} \tag{89}$$

The inlet area A_{in} is the upstream burning surface area and the outlet area A_{out} is the cross-sectional area of the chamber at the specified axial location. FlightStream®'s velocity was taken at the centerline rather than averaging across the outlet to avoid the known error near the mesh surfaces (refer to velocity contour figures in analytic section). Figure 19 shows FlightStream®'s centerline velocity compared to the one-dimensional flow.

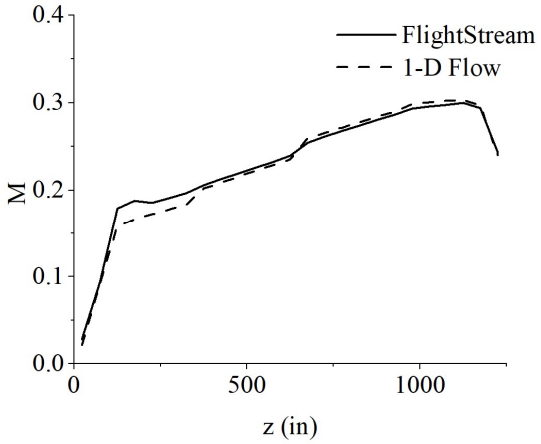

Fig. 19 Results from the continuity analysis.

As expected, FlightStream®'s solution is very near the one-dimensional flow solution. Just aft of the finned section (approximately 175 inches downstream), FlightStream® has higher Mach numbers than the one-dimensional flow, indicating that the mass flow is more concentrated near the central axis. One-dimensional flow is a good approximation to compare FlightStream®'s results to, but the solution can be further validated with a streamtube analysis.

FlightStream®'s solution should be entirely isentropic, as there are no irreversibilities present in the irrotational and inviscid flow; a streamtube analysis was conducted to confirm this. A streamtube is a collection of streamlines that form a tubular region of fluid. Because fluid flows tangent to every point along a streamline, no flow crosses through a streamtube. For this reason, the cross-sectional area and Mach profile of a given streamtube should follow isentropic theory. A streamline near the centerline was chosen and discrete points were defined along its length. Assuming axisymmetric flow, the streamline was "revolved" around the central axis to create a streamtube of circular cross-section. Data near the central axis was used to avoid the known error near mesh surfaces and noncircular streamtube cross-sections in the finocyl section. At each of the discrete points defined along the streamline, the Mach number and streamtube's cross-sectional area were recorded. These values were compared to the area-Mach relation from isentropic flow theory, shown as Eq. (90). A reference point near the headwall was used, denoted by the subscript "h", as there is no choke point in FlightStream®'s solution.

$$\frac{A}{A_h} = \frac{M_h}{M}\left(\frac{1+\frac{\gamma-1}{2}M^2}{1+\frac{\gamma-1}{2}{M_h}^2}\right)^{\frac{\gamma+1}{2(\gamma-1)}} \tag{90}$$

The results are shown in Fig. 20; as expected, the flow is isentropic throughout the entire chamber. The results of the streamtube and continuity analysis indicate the internal flowfield of the RSRM model in FlightStream® is valid. Please note that this is a verification of the

mathematical solution to the equations of fluid motion per assumptions and is not intended to be a validation of the physical flow solution.

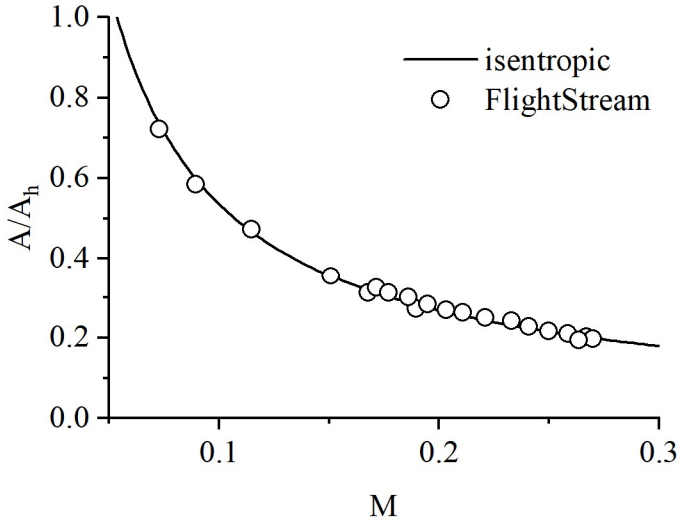

Fig. 20 Results from the streamtube analysis.

To compare with experimental data and other computational models, the rotational and compressibility corrections previously outlined were applied. The Mach profile increased by approximately 3% by applying the customized inlet condition and the compressibility correction increased it further by approximately 5%. The results are presented in the figures below compared to SHARP, a fully coupled Navier-Stokes solver developed at Thiokol, and a one-dimensional code developed at Thiokol known as SCB02.[51] The pressure plot includes data from the RSRM qualification motors QM-7 and QM-8. The data from the qualification motors was scaled to account for the difference in the propellants' initial temperature and burn rate.

It was found that the irrotational solution is more accurate in the finocyl section than applying the correction. This could be because there is very little vorticity in the central bore of the finocyl, or it could be that the rotational correction that was used does not apply to the

finocyl geometry. Thus, the flow in the finocyl section was left irrotational and the correction was applied at its outlet (approximately 175 inches) onward.

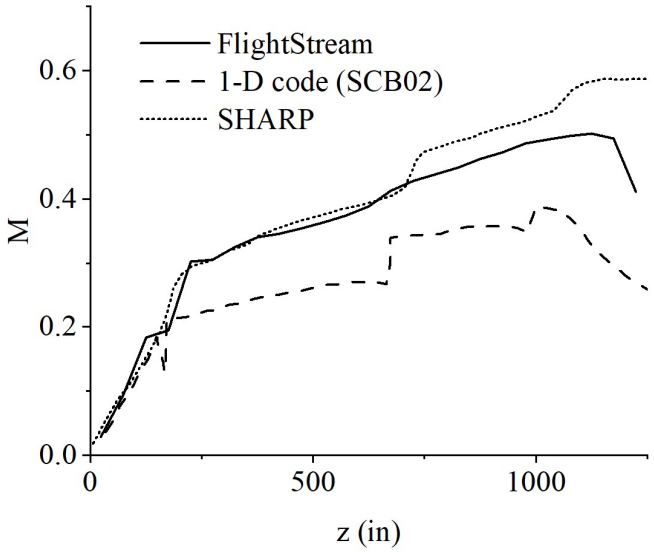

Fig. 21 Centerline Mach profile in the RSRM.

FlightStream®'s Mach profile matches the SHARP code in the first two segments of the RSRM exceptionally well. The slot between the first and second segments (at approximately 350 inches) is smaller than the other slots at this stage in the motor's operation and does not have much influence on the flow. In both SCB02 and SHARP, two rapid increases in the Mach number occur at axial locations of approximately 700 inches and 1000 inches; this is caused by the slots at these locations forward and aft of the third motor segment. FlightStream®'s solution does not observe this effect and the solution diverges from the validation data. This is because the slots have a much larger influence on rotational flow than irrotational flow. In a rotational flow, a recirculation zone forms on the aft side of the slot, essentially restricting the bulk flow and increasing the mass flow rate.[4] In irrotational flow, the slots are virtually thin strips along the burning surface of slightly increased mass addition. These effects will clearly not materialize

in FlightStream®'s results considering the rotational correction in this analysis is simply an augmentation to the irrotational solution.

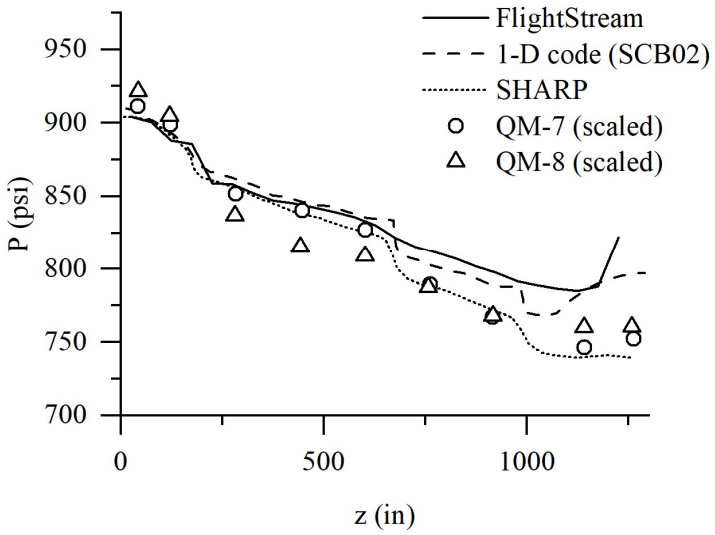

Fig. 22 Centerline pressure profile in the RSRM.

The pressure plot features experimental data from QM-7 and QM-8 qualification motors, of which the QM-7 data in the first two segments agrees well with FlightStream®'s solution. The sharp increase in FlightStream®'s results seen at the exit of the motor is likely because no nozzle geometry was included in the model. The rotational correction that was applied is also only suited for small taper angles; it is possible the rotational flow in the much larger taper of the aft section cannot be represented well by the correction. Again, the pressure disunites from the QM-7 data upon reaching the second grain slot. Considering FlightStream®'s solution is potential and only two simple corrections were applied, the results agree remarkably well with the experimental data and the more rigorous SHARP model. One could expect highly accurate results using this method to model the internal flow of a motor that does not contain grain slots such as in the RSRM.

4 Conclusion

The objective of this thesis was to investigate FlightStream®'s potential for internal flow applications; the work presented indicates FlightStream® is indeed viable for such. The analytic validations all showed good agreement with FlightStream®, besides expected error near the mesh surfaces and the slight error observed along the centerline of the planar models. Research in Flight is currently working on a vortex-splitting method to address the error caused by the vortex singularities at the mesh surface. The error observed in the planar models could be attributed to the finite width of the models. Despite the complex internal environment of the RSRM, FlightStream® was able to reproduce accurate Mach and pressure profiles with only two simple flow corrections. Divergence between FlightStream®'s solution and the validation data of the RSRM was observed at two of the three grain slots in the model, presumably due to recirculation regions that were not captured in the method used. A potential solution for this is discussed in the following section.

4.1 Recommendations and Future Work

The validation studies conducted in this report serve as foundational work in which a wide range of further studies can be confidently conducted with FlightStream®. Moving forward with this work, it would be valuable to couple grain regression with FlightStream®. Doing so would allow for the production of thrust-time profiles from FlightStream®, which are incredibly important in motor design. This time-based evolution of the combustion chamber could also be used with erosive burning models to investigate erosive burning's effect on flow properties. Other internal flow scenarios, such as hybrid rockets, should be explored as well. FlightStream®'s irrotational solution may prove to be more useful in hybrid rocket applications wherein diffusive burning occurs.

The greatest limitation of FlightStream® currently regarding internal flow is that the solution is irrotational. Perhaps there are better methods than the one used in this report to approximate, or fully incorporate, rotational flow in FlightStream®. A possible solution is the use of "vortex walls", or boundaries defined by recirculating flow that act as impermeable walls to the potential solution. These were used in conjunction with a potential solver by Smith-Kent et al. to better model the cavity formed around a submerged nozzle.[41] Vortex walls could possibly be used in a similar way in FlightStream® to better capture the effects of grain slots like in the RSRM. The difficulty in using this technique is accurately determining the shape of the recirculation zones. Also, it may be difficult to incorporate these over burning surfaces, as you would need an additional model to represent the mass transfer across the wall. In the referenced report, the vortex wall's geometry was determined through empirical means and were used over a non-burning surface.

Acoustic studies can greatly benefit from the geometrical flexibility FlightSteam® offers and is a worthwhile direction for future work. Many past analytic studies that have been severely geometrically limited could use FlightStream®'s solutions as a basis to expand the studies to more complex geometries. Multidisciplinary design analysis and optimization is also a reasonable direction for future studies, given the speed at which solutions can be obtained using FlightStream® and the usefulness of optimization in early design. In such work, FlightStream® can rapidly produce solutions for a variety of parameter modifications enabling sensitivity analyses and response surface generation in a design of experiments method.

References

[1] Parker, K., & Summerfield, M. (1964). The ignition transient in solid propellant rocket motors. *Solid Propellant Rocket Conference*. https://doi.org/10.2514/6.1964-126

[2] Taylor, G. I., "Fluid Flow in Regions Bounded by Porous Surfaces," *Proceedings of the Royal Society of London, Series A,* Vol. 234, No. 1199, 1956, pp. 456-475. doi: 10.1098/rspa.1956.0050

[3] Sutton, G. P., & Biblarz, O. (2017). *Rocket propulsion elements*. Wiley.

[4] Hilbing, J., & Heister, S. (1993). Radial slot flows in solid rocket motors. *29th Joint Propulsion Conference and Exhibit*. https://doi.org/10.2514/6.1993-2309

[5] Courta, A. (1995). Vortex shedding in solid rocket motors. *33rd Aerospace Sciences Meeting and Exhibit*. https://doi.org/10.2514/6.1995-727

[6] Messner, A. M. (1985). Grain deformation of gas flow passages in solid rocket motors. *Journal of Propulsion and Power*, *1*(6), 498–500. https://doi.org/10.2514/3.22835

[7] Chen, Y., Guildenbecher, D. R., Hoffmeister, K. N. G., Cooper, M. A., Stauffacher, H. L., Oliver, M. S., & Washburn, E. B. (2017). Study of aluminum particle combustion in solid propellant plumes using digital in-line holography and imaging pyrometry. *Combustion and Flame*, *182*, 225–237. https://doi.org/10.1016/j.combustflame.2017.04.016

[8] JasperLal, C., Sridharan, P., Krishnaraj, K., & Srinivasan, V. (2013). Investigation of Slag Accumulation in Solid Rocket Motors. *49th AIAA/ASME/SAE/ASEE Joint Propulsion Conference*. https://doi.org/10.2514/6.2013-3861

[9] Mikkelsen, C., & Roys, G. (1982). Application of the Saderholm erosive burning model to nozzleless solid propellant rocket motors. *18th Joint Propulsion Conference*. https://doi.org/10.2514/6.1982-1146

[10] Wang, Q. (2003). Development of Erosive Burning Models for CFD Predictions of Solid Rocket Motor Internal Environments. *39th AIAA/ASME/SAE/ASEE Joint Propulsion Conference and Exhibit*.

[11] Fuchs, M., Aharon, I., & Bar-Gill, M. (1988). Cold-flow and full scale testing of an ejecta pulser for solid propellant rocket motors. *24th Joint Propulsion Conference*. https://doi.org/10.2514/6.1988-3297

[12] Culick, F. E. C., "Rotational Axisymmetric Mean Flow and Damping of Acoustic Waves in a Solid Propellant Rocket," *AIAA Journal,* Vol. 4, No. 8, 1966, pp. 1462-1464.

[13] Majdalani, J., & Saad, T. (2007). The Taylor-Culick profile with arbitrary headwall injection. *Physics of Fluids*, *19*(9), 093601. https://doi.org/10.1063/1.2746003

[14] Majdalani, J. (2005). The Compressible Taylor-Culick Flow. *41st AIAA/ASME/SAE/ASEE Joint Propulsion Conference & Exhibit*. https://doi.org/10.2514/6.2005-3542

[15] Sams, O. C., Majdalani, J., & Saad, T. (2007). Mean Flow Approximations for Solid Rocket Motors with Tapered Walls. *Journal of Propulsion and Power*, *23*(2), 445–456. https://doi.org/10.2514/1.15831

[16] Sams, O., Majdalani, J., & Flandro, G. (2003). Mean Flow Approximation for a Slab Rocket Motor with Tapered Sidewalls. *39th AIAA/ASME/SAE/ASEE Joint Propulsion Conference and Exhibit*. https://doi.org/10.2514/6.2003-5114

[17] Majdalani, J., Vyas, A. B., and Flandro, G. A., "Higher Mean-Flow Approximation for a Solid Rocket Motor with Radially Regressing Walls," AIAA Journal, Vol. 40, No. 9, 2002, pp. 1780–1788.

[18] Hart, R. W., and McClure, F. T., "Combustion Instability: Acoustic Interaction with a Burning Propellant Surface," *The Journal of Chemical Physics,* Vol. 30, No. 6, 1959, pp. 1501-1514. doi: 10.1063/1.1730226

[19] Hart, R. W., and McClure, F. T., "Theory of Acoustic Instability in Solid-Propellant Rocket Combustion," *Tenth Symposium (International) on Combustion,* Vol. 10, No. 1, 1965, pp. 1047-1066. doi: 10.1016/S0082-0784(65)80246-6

[20] Saad, T., and Majdalani, J., "On the Lagrangian Optimization of Wall-Injected Flows: From the Hart–McClure Potential to the Taylor–Culick Rotational Motion," *Proceedings of the Royal Society of London, Series A,* Vol. 466, No. 2114, 2010, pp. 331-362.

[21] Maicke, B. A., Saad, T., & Majdalani, J. (2012). On the compressible Hart-McClure and Sellars mean flow motions. *Physics of Fluids*, *24*(9), 096101. https://doi.org/10.1063/1.4748349

[22] Coats, D., Nickerson, G., Dang, A., Dunn, S., & Kehtarnavazs, H. (1987). Solid performance program (SPP). *23rd Joint Propulsion Conference*. https://doi.org/10.2514/6.1987-1701

[23] Lamberty, J. (1981). A report on the grain design and internal ballistic module of the improved solids performance program. *19th Aerospace Sciences Meeting*. https://doi.org/10.2514/6.1981-34

[24] Isfahani, A., Zhang, J., & Jackson, T. (2009). DNS Simulation of Erosive Burning in Planar Periodic Rockets. *47th AIAA Aerospace Sciences Meeting Including The New Horizons Forum and Aerospace Exposition*. https://doi.org/10.2514/6.2009-805

[25] Sabnis, J. S., Gibeling, H. J., & McDonald, H. (1989). Navier-Stokes analysis of solid propellant rocket motor internal flows. *Journal of Propulsion and Power*, *5*(6), 657–664. https://doi.org/10.2514/3.23203

[26] Hsieh, K. C., Yang, V., & Tseng, I. S. (1988). Navier-Stokes calculation of solid-propellant rocket motor internal flowfields. *24th Joint Propulsion Conference*. https://doi.org/10.2514/6.1988-3182

[27] Unnikrishnan, C., Sana, V., & Raghunandan, B. (2001). Internal flow simulation of solid rockets using an unsteady Navier Stokes solver. *37th Joint Propulsion Conference and Exhibit*. https://doi.org/10.2514/6.2001-3450

[28] Paoli, R., Poubeau, A., & Cariolle, D. (2020). Large-Eddy Simulations of a Reactive Solid Rocket Motor Plume. *AIAA Journal*, *58*(4), 1639–1656. https://doi.org/10.2514/1.j058601

[29] Bernardini, M., Cimini, M., Stella, F., Cavallini, E., Di Mascio, A., Neri, A., & Martelli, E. (2020). Large-Eddy Simulation of Vortex Shedding and Pressure Oscillations in Solid Rocket Motors. *AIAA Journal*, *58*(12), 5191–5201. https://doi.org/10.2514/1.j058866

[30] Dick, W., Fiedler, R., & Heath, M. (2006). Building Rocstar: Simulation Science for Solid Propellant Rocket Motors. *42nd AIAA/ASME/SAE/ASEE Joint Propulsion Conference & Exhibit*. https://doi.org/10.2514/6.2006-4590

[31] Brandyberry, M., Fiedler, R., & McLay, C. (2005). Verification and Validation of the Rocstar 3-D Multi-physics Solid Rocket Motor Simulation Program. *41st AIAA/ASME/SAE/ASEE Joint Propulsion Conference & Exhibit*. https://doi.org/10.2514/6.2005-3992

[32] Gale, M. P., Alam, M. F., Mehta, R., & Luke, E. (2020). Multiphase Modeling of Solid Rocket Motor Internal Environment. *AIAA Propulsion and Energy 2020 Forum*. https://doi.org/10.2514/6.2020-3934

[33] Bianchi, D., & Neri, A. (2015). Numerical Simulation of Chemical Erosion in VEGA Launcher Solid-Propellant Rocket Motor Nozzles. *51st AIAA/SAE/ASEE Joint Propulsion Conference*. https://doi.org/10.2514/6.2015-4175

[34] King, M. K. (1977). A Model of Erosive Burning of Composite Propellants. https://doi.org/10.21236/ada040459

[35] Rout, R., Mukunda, H., & Jain, V. (1978). Erosive burning characteristics of solid propellant rocket motor. *14th Joint Propulsion Conference*. https://doi.org/10.2514/6.1978-1097

[36] Hegab, A. (2007). AN OVERVIEW OF SOLID PROPELLANT COMBUSTION MODELING. *International Conference on Aerospace Sciences and Aviation Technology*, *12*(ASAT CONFERENCE), 1–24. https://doi.org/10.21608/asat.2007.23875

[37] McClure, F. T., Hart, R. W., & Cantrell, R. H. (1963). Interaction Between Sound and Flow: Stability of T-Burners. *AIAA Journal*, *1*(3), 586–590. https://doi.org/10.2514/3.54846

[38] Terrill, R. M., & Colgan, T. (1991). Some simple analytic solutions of the Navier-Stokes equations. *International Journal of Engineering Science*, *29*(1), 55–68. https://doi.org/10.1016/0020-7225(91)90076-f

[39] Haloulakos, V. E. (1991). Slag mass accumulation in spinning solid rocket motors. *Journal of Propulsion and Power*, *7*(1), 14–21. https://doi.org/10.2514/3.23288

[40] Majdalani, J., & Saad, T. (2012). Internal Flows Driven by Wall-Normal Injection. *Advanced Fluid Dynamics*. https://doi.org/10.5772/25839

[41] Smith-Kent, R., Perkins, F., & Abel, R. (1993). A potential, two-phase flow model for predicting solid rocket motor slag. *29th Joint Propulsion Conference and Exhibit*. https://doi.org/10.2514/6.1993-2307

[42] King, L., Hartfield, R. J., & Ahuja, V. (2015). Aerodynamic Optimization of Integrated Wing-Engine Geometry using an Unstructured Vorticity Solver. *33rd AIAA Applied Aerodynamics Conference*. https://doi.org/10.2514/6.2015-2880

[43] Sandoz, B., Ahuja, V., & Hartfield, R. J. (2018). Longitudinal Aerodynamic Characteristics of a V/STOL Tilt-wing Four-Propeller Transport Model using a Surface Vorticity Flow Solver. *2018 AIAA Aerospace Sciences Meeting*. https://doi.org/10.2514/6.2018-2070

[44] Apte, S., & Yang, V. (2002). Unsteady Flow Evolution in Porous Chamber with Surface Mass Injection, Part 2: Acoustic Excitation. *AIAA Journal*, *40*(2), 244–253. https://doi.org/10.2514/2.1666

[45] Fabignon, Y., Dupays, J., Avalon, G., Vuillot, F., Lupoglazoff, N., Casalis, G., & Prévost, M. (2003). Instabilities and pressure oscillations in solid rocket motors. *Aerospace Science and Technology*, *7*(3), 191–200. https://doi.org/10.1016/s1270-9638(02)01194-x

[46] Flandro, G. A., Fischbach, S. R., & Majdalani, J. (2007). Nonlinear rocket motor stability prediction: Limit amplitude, triggering, and mean pressure shift. *Physics of Fluids*, *19*(9), 094101. https://doi.org/10.1063/1.2746042

[47] Boyer, G., Casalis, G., & Estivalèzes, J. L. (2013). Stability and sensitivity analysis in a simplified solid rocket motor flow. *Journal of Fluid Mechanics*, *722*, 618–644. https://doi.org/10.1017/jfm.2013.90

[48] Ahuja, V., & Hartfield, R. (2015). Predicting the Aero Loads Behind a Propeller in the Presence of a Wing Using Flightstream. *15th AIAA Aviation Technology, Integration, and Operations Conference*. https://doi.org/10.2514/6.2015-2734

[49] Ahuja, V. (2013). *Aerodynamic Loads Over Arbitrary Bodies By Method Of Integrated Circulation* (dissertation).

[50] Ahuja, V., & Hartfield, R. J. (2016). Aerodynamic Loads over Arbitrary Bodies by Method of Integrated Circulation. *Journal of Aircraft*, *53*(6), 1719–1730. https://doi.org/10.2514/1.c033619

[51] Laubacher, B. (2000). Internal flow analysis of large L/D solid rocket motors. *36th AIAA/ASME/SAE/ASEE Joint Propulsion Conference and Exhibit*. https://doi.org/10.2514/6.2000-3803

[52] Wasistho, B., Fiedler, R., Namazifard, A., & Brandyberry, M. (2005). 3-D Coupled Simulations of Flexible Inhibitors in the RSRM. *41st AIAA/ASME/SAE/ASEE Joint Propulsion Conference & Exhibit*. https://doi.org/10.2514/6.2005-3996

[53] Majdalani, J., & Fist, A. (2014). Improved Mean Flow Solution for Solid Rocket Motors with a Naturally Developing Swirling Motion. *50th AIAA/ASME/SAE/ASEE Joint Propulsion Conference*. https://doi.org/10.2514/6.2014-4016

[54] Volume III, Design, Development and Verification Proposal, TWP 077326, Submitted to NASA George C. Marshall Space Flight Center by Wasatch Division Thiokol Chemical Corporation, 1973.

[55] Dick, W., Heath, M., Fiedler, R., & Brandyberry, M. (2005). Advanced Simulation of Solid Propellant Rockets from First Principles. *41st AIAA/ASME/SAE/ASEE Joint Propulsion Conference & Exhibit*. https://doi.org/10.2514/6.2005-3990